# CHARACTERIZATION OF HEAT TREATED BISMUTH-INDIUM THIN FILMS

by

Mahshid Karimi

B. A. Sc., Shiraz University, Iran 1994

THESIS SUBMITTED IN PARTIAL FULFILLMENT OF THE REQUIREMENTS FOR THE DEGREE OF

MASTER OF SCIENCE

In the Department of Physics

© Mahshid Karimi 2005

SIMON FRASER UNIVERSITY

Spring 2005

Copyrights are not reserved.
Permission is hereby granted to
reproduce this work in whole or in part.

# APPROVAL

| | |
|---|---|
| **Name:** | Mahshid Karimi |
| **Degree:** | MASTER OF PHYSICS |
| **Title of Thesis:** | Characterization of Heat Treated Bismuth - Indium Thin Films |
| **Examining Committee:** | Dr. Howard D. Trottier; Professor (Chair) |
| | Dr. Karen L. Kavanagh, Professor, Senior Supervisor |
| | Dr. Simon Watkins, Professor, Supervisor |
| | Dr. Barbara Frisken, Professor, Supervisor |
| | Dr. Glenn Chapman, Professor, Examiner |
| **Date Approved:** | April 12, 2005 |

# SIMON FRASER UNIVERSITY

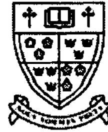


# PARTIAL COPYRIGHT LICENCE

The author, whose copyright is declared on the title page of this work, has granted to Simon Fraser University the right to lend this thesis, project or extended essay to users of the Simon Fraser University Library, and to make partial or single copies only for such users or in response to a request from the library of any other university, or other educational institution, on its own behalf or for one of its users.

The author has further granted permission to Simon Fraser University to keep or make a digital copy for use in its circulating collection.

The author has further agreed that permission for multiple copying of this work for scholarly purposes may be granted by either the author or the Dean of Graduate Studies.

It is understood that copying or publication of this work for financial gain shall not be allowed without the author's written permission.\

Permission for public performance, or limited permission for private scholarly use, of any multimedia materials forming part of this work, may have been granted by the author. This information may be found on the separately catalogued multimedia material and in the signed Partial Copyright Licence.

The original Partial Copyright Licence attesting to these terms, and signed by this author, may be found in the original bound copy of this work, retained in the Simon Fraser University Archive.

W. A. C. Bennett Library
Simon Fraser University
Burnaby, BC, Canada

# Abstract

Two layer sputtered Bi/In thin films (12-120 nm/layer) act as a micro-fabrication resist with many potential applications. Their physical, chemical, and optical characteristics change after laser exposures that produce a rapid thermal anneal in selected areas. Laser exposed areas have lower reflectivity and higher transparency. The structural and electrical properties of Bi/In films before and after annealing was investigated in this thesis work. AFM (Atomic Force Microscopy), XRD (X-ray Diffraction), and TEM (Transmission Electronic Microscopy) show that the as-deposited films are polycrystalline, continuous, but with a rough, island morphology. Furnace or laser anneals in air result in the formation of Bismuth and Indium oxides. The island morphology is maintained but there is evidence of melting and recrystallization. RBS (Rutherford Back Scattering) and NRA (Nuclear Reaction Analysis) analysis confirm that Bi/In films exposed to laser or furnace contain a large fraction of oxygen consistent with the XRD, and TEM results. Hall effect measurements show a high electron carrier concentrations of $4 \times 10^{20} cm^{-3}$ for Bi/In films after exposure.

*To My Little Qianah,*

*"Your hands are like two wings which let me fly as high as you are with me".*

*To My Husband Abbas,*
*Who Encouraged me to* **Never Give Up.**

# Acknowledgments

I would like to thank Prof. Karen Kavanagh for being an excellent advisor and teacher. Special thanks are extended to : Prof. Glenn Chapman; Dr. Richard Yuqiang Tu for being my teammate and for their helpful suggestions and preparation of the samples for this project; Dr. W. Lennard at University of Western Ontario for RBS measurements; Dr. Saeid Kamal and Christina Kaiser for their points in writing, and Nasim Morawej for her assistance in data collection.

This work was supported in part by the BC Advanced Systems Institute and NSERC.

# Contents

**Approval** ii

**Abstract** iii

**Dedication** iv

**Acknowledgments** v

**Contents** vi

**List of Tables** ix

**List of Figures** xi

**1 Introduction** 1

1.1 Motivation for this Work . . . . . . . . . . . . . . . . . . . . . . . . 1

1.2 Microlithography . . . . . . . . . . . . . . . . . . . . . . . . . . . . 2

1.2.1 Organic Photoresist . . . . . . . . . . . . . . . . . . . . . . . . 3

1.2.2 Inorganic Resists . . . . . . . . . . . . . . . . . . . . . . . . . 3

1.3 Thesis Outline . . . . . . . . . . . . . . . . . . . . . . . . . . . . . 5

**2 Experimental Procedures** 7

2.1 Structural Properties . . . . . . . . . . . . . . . . . . . . . . . . . 7

2.2 Sample Preparation . . . . . . . . . . . . . . . . . . . . . . . . . . 7

2.2.1 Thin Films . . . . . . . . . . . . . . . . . . . . . . . . . . . . 7

2.2.2 Bulk BiIn Alloys . . . . . . . . . . . . . . . . . . . . . . . . . 10



I

2.3 Principles of X-Ray Diffraction . . . . . 11
2.4 TEM (Transmission Electron Microscopy) . . . . . 13
2.4.1 Modes of Operation . . . . . 13
2.4.2 Scanning TEM (STEM) . . . . . 14
2.4.3 Sample Thinning for TEM . . . . . 14
2.5 Surface morphology . . . . . 17
2.5.1 Scanning Electron Microscopy (SEM) . . . . . 17
2.5.2 Atomic Force Microscopy (AFM) . . . . . 17
2.6 Material Composition . . . . . 18
2.6.1 Rutherford Backscattering Spectrometry . . . . . 18
2.7 Electrical Properties . . . . . 19
2.7.1 Hall Measurements . . . . . 19
2.7.2 van der Pauw Theory . . . . . 20
2.7.3 Experimental Hall Setup . . . . . 21
2.7.4 Four–Point Probe . . . . . 22

**3 Results and Discussion** **23**
3.1 Structural Properties . . . . . 23
3.1.1 XRD Results – Thin Films . . . . . 23
3.1.2 XRD Results – Bulk Alloy . . . . . 24
3.1.3 TEM Results . . . . . 30
3.2 Surface Morphology . . . . . 38
3.2.1 SEM Results . . . . . 38
3.2.2 AFM Results . . . . . 44
3.3 Material Composition . . . . . 48
3.3.1 RBS Results . . . . . 48
3.4 Electrical Properties . . . . . 57

**4 Summary** **59**
4.1 Summary of structural properties . . . . . 59
4.2 Comparison of IBO to Indium Tin Oxide . . . . . 60
4.3 Future Work . . . . . 63

**A** **68**

# List of Tables

2.1 List of sputtered-deposited samples investigated. . . . . . . . . . . . . . . 9

2.2 Properties of bismuth and indium [10, 11]. . . . . . . . . . . . . . . . . . . . 10

3.1 AFM data for as-deposited and annealed films on silicon substrates and glass 52

3.2 RBS/NRA results of oxygen concentration in 120/120 nm Bi/In/Si samples. 54

3.3 Hall measurement comparison of ITO and Laser annealed BiIn . . . . . . . 57

3.4 Four-point probe sheet resistance and resistivity measurements [25] . . . . 58

A.1 Summary and analysis of X-ray data from Fig. 3.1 0.9W laser-annealed BiIn thin films (12/12 nm) on Si (001). The database numbers are from JCPDS-ICDD (1993). . . . . . . . . . . . . . . . . . . . . . . . . . . . . 69

A.2 Summary and analysis of the XRD data from Fig. 3.1 Bi/In films on Si(001), (a) as-deposited, (b) 2.5 W , and (c) 3.2W laser-annealed sample. Data calibration based on the Si(004) peak. The database are from JCPDS-ICDD (1993). . . . . . . . . . . . . . . . . . . . . . . . . . . . . 70

A.3 Summary of the data from Fig. 3.2 as-deposited BiIn thin film (45/45 nm) on (Si(001), Si(111), $SiO_2$/Si(001), and $Si_3N_4$/Si(001). The database numbers are from JCPDS-ICDD (1993). . . . . . . . . . . . . . . . . . . . . 71

A.4 Summary and analysis of X-ray data from Fig. 3.3 laser-annealed, BiIn thin film (45/45 nm) on silicon substrates Si (001), Si(111), $SiO_2$/Si (001), $Si_3N_4$/Si (001) and glass. The database are from JCPDS-ICDD (1993). . . . 72

A.5 Summary and analysis of X-ray data from Fig. 3.4 as-deposited Bi/In on Si (001) (45/45 nm). The data calibration is based on Si (004) or Si (111) peak positions. The database numbers are from JCPDS-ICDD (1993). . . . 73

A.6 Summary and analysis of XRD measurements of as-deposited (45/45 nm -90/90 nm) Bi/In for 3 substrates (glass, Si(001), Si(111) Fig. 3.4. Calibration based on the substrate Si(004). The database numbers are from JCPDS-ICDD (1993). . . . . . . . . . . . . . . . . . . . . . . . . . . 74

A.7 Summary and analysis of XRD measurements from laser-annealed Bi/In of Fig. 3.5 for 3 substrates (glass, Si(001), Si(111)) in different fabrication time. Data calibration based on Si peak. The database numbers are from JCPDS-ICDD (1993). . . . . . . . . . . . . . . . . . . . . . . . . . . 76

A.8 X - ray summary and analysis of low temperature bulk melt of Bi and In in $N_2$, Bi and In pieces melted at 270°C . The database numbers are from JCPDS-ICDD (1993). . . . . . . . . . . . . . . . . . . . . . . . . . . 77

A.9 XRD summary and analysis of heated BiIn (50 %) solid metals in air, at 270°C. The database numbers are from JCPDS-ICDD (1993). . . . . . . . 78

A.10 Electron diffraction pattern analysis of the SAD data in Fig. 3.8. Data calibration was based on a GaAs sample. The phase database numbers are from JCPDS-ICDD (1993). . . . . . . . . . . . . . . . . . . . . . . . . 79

A.11 (b) Analysis of the SAD shown in Fig. 3.9. Furnace-annealed 150°C on SiO grid. The database numbers are from JCPDS-ICDD (1993). . . . . . . 80

A.12 (c)Analysis of the SAD shown in Fig. 3.10. Furnace-annealed sample at 200 °C on SiO grid. The database numbers are from JCPDS-ICDD (1993). 81

A.13 (d) Analysis of the SAD shown in Fig. 3.11. Furnace-annealed sample at 246 °C on SiO grid. The database numbers are from JCPDS-ICDD (1993). 82

A.14 (e) Analysis of the SAD shown in Fig. 3.12. Laser-annealed Bi/In on Si Ion milled. . . . . . . . . . . . . . . . . . . . . . . . . . . . . . . 83

# List of Figures


1.1 Bi-In phase diagram [7]. . . . . . . . . . . . . . . . . . . . . . . . . . . 2

1.2 A simplified example of the microfabrication process, by permission, [5]. . 4

1.3 A dry bimetallic thermal resist process. (a) shows the substrate and the layer to be patterned. (b) In and Bi have been sputtered onto the substrate. (c) UV exposure converts the exposed area into an alloy, which has different chemical properties from the unexposed area. (d) The development process removes the unexposed and retains the exposed area. (e) The pattern is transferred to the underlying layer by either plasma or wet etch. (f) The whole process is completed by etching the exposed resist, by permission, [5]. 6

2.1 Schematic of an X-ray powder diffractometer, by permission [16]. . . . . . 12

2.2 Optical photographs of increasing magnification of 12/12 nm BiIn as deposited on 300 mesh, lacy carbon support grid ($10 \times 10$ $\mu$m grid size). In some regions the lacy carbon is interconnected by the film but mainly there is no film left across the holes. . . . . . . . . . . . . . . . . . . . . . . . . 16

2.3 Hall bar and van der Pauw sample schematics. In both schematics the current $I_{BD}$ and a magnetic field B produces a Hall voltage $V_{AC}$. From a measurement of the Hall voltage ($V_{AC}$) for a known current ($I_{BD}$) and magnetic field (B) the net carrier concentration can be determined, by permission, [13]. 22

3.1 (a) XRD scans of (i) as deposited (ii) laser annealed (0.9W) Bi/In (12/12 nm) films on Si(001) (sample A, Table 2.1). (b) XRD scans of (12/12 nm) Bi/In films on Si (001), (i) as-deposited, and laser annealed in air with (ii) 2.5 W and (iii) 3.2 W power (sample B, Table2.1). The marked (•) indium oxide is referring to the rhombohedral structure of this alloy and unmarked one is refereing to the cubic structure. . . . . . . . . . . . . . . . . . . . 25

3.2 XRD scans of as-deposited Bi/In (45/45 nm) films on (a) Si(111) (b) Si(001), (c) $Si_3N_4$/ Si(001), (d) $SiO_2$/ Si(001), and (e) glass, substrates. . . . . . . . 26

3.3 XRD scans from laser annealed of 45/45 nm Bi/In film of Fig. 3.2 on (a) Si(111) (b) Si(001), (c) $Si_3N_4$/ Si(001), (d) $SiO_2$/ Si(001), and (e) glass substrates (sample C, Table 2.1). This figure shows the same structural formation after annealing for the Si substrates but glass is different. The marked (•) indium oxide refers to the rhombohedral structure of this alloy and unmarked one refers to the cubic structure. . . . . . . . . . . . . . . . 27

3.4 XRD scans from as-deposited Bi/In film deposited on (a) glass 90/90 nm, (b) Si (001) 120/120 nm, and (c) Si (111) 45/45 nm (samples D, E, F in Table 2.1) . . . . . . . . . . . . . . . . . . . . . . . . . . . . . . . 28

3.5 XRD scans of the same films in Fig. 3.4 after laser-annealing in air at 0.9 W laser power, (a) glass 90/90 nm, and (b) Si (100) 120/120 nm and (c) Si(111) 45/45 nm (samples D, E, F in Table 2.1). The marked (•) indium oxide is refers to the rhombohedral structure of this alloy and the unmarked one is refers to the cubic structure. . . . . . . . . . . . . . . . . . . . . . 29

3.6 XRD data of solid In/Bi melted in $N_2$ by heating to 270°C and cooling to room temperature in (a) $N_2$ and (b) in air. The marked (•) indium oxide is refers to the rhombohedral structure of this alloy and the unmarked one is refers to the cubic structure. . . . . . . . . . . . . . . . . . . . . . . . . 31

3.7 TEM planview and SAD images from an ion milled 12/12 nm Bi/In laser-annealed in air but damaged by ion milling. The SAD shows only poly - Si diffraction. . . . . . . . . . . . . . . . . . . . . . . . . . . . . . . . . . 32

3.8 TEM BF image with corresponding SAD: 12/12 nm Bi/In as-deposited on SiO support grid. . . . . . . . . . . . . . . . . . . . . . . . . . . . . 33

3.9 TEM BF image with corresponding SAD of 12/12 nm Bi/In on carbon support grid heated in a furnace at 150 °C. . . . . . . . . . 34
3.10 TEM BF image with corresponding SAD of 12/12 nm Bi/In on carbon support grid heated in furnace at 200 °C. . . . . . . . . . 35
3.11 TEM BF image with corresponding SAD of BiIn, on SiO support grid furnace-annealed at 246 °C. . . . . . . . . . 36
3.12 TEM planview image and SAD from an ion milled 12/12 nm Bi/In film on Si(001) laser-annealed in air. . . . . . . . . . 37
3.13 (a) High angle annular dark field (HAADF) image, (b) EDS spectra from one spot, (c) HAADF intensity along indicated line in image, (d) results of EDS along the line for Bi, In, and O. . . . . . . . . . 39
3.14 SEM image of BiIn (12/12 nm) on Si(001) (a) as-deposited and heated at (b) 150°C and (c) 200°C (e-beam voltage 5kV). . . . . . . . . . 40
3.15 SEM image of a Bi/In (45/45 nm) on Si(001) (a) as-deposited and (b) laser-annealed (e-beam voltage 15 kV). . . . . . . . . . 41
3.16 SEM image of BiIn (45/45 nm) on $Si_3N_4$/Si(001) (a) as-deposited and (b) laser-annealed (e-beam voltage 12 kV). . . . . . . . . . 42
3.17 SEM image of BiIn (45/45 nm) on $SiO_2$/Si(001) (a) as-deposited and (b) laser-annealed (e-beam voltage 15 kV). . . . . . . . . . 43
3.18 SEM image of BiIn as-deposited (45/45 nm) on glass (e-beam 15kV). . . . 45
3.19 SEM image of BiIn (45/45 nm) on glass at the border of laser-annealed and as-deposited regions (e-beam voltage 15 kV). . . . . . . . . . 45
3.20 SEM image of BiIn (45/45 nm) on at the border of laser annealed and as-deposited regions (E-beam voltage 5kV) for (a) $SiO_2$/Si(001) and (b) Si(001) (e-beam voltage 5 kV). . . . . . . . . . 46
3.21 Non-contact AFM images of 90 nm (45/45 nm) Bi/In as-deposited and laser-annealed film on (a) $SiO_2$/ Si(001) and (b) glass substrate. . . . . . . 47
3.22 Height analysis of AFM data from as-deposited Bi/In film on top of glass, fig. 3.21 (b) . . . . . . . . . . 48
3.23 Height analysis of laser-annealed Bi/In film on a $SiO_2$Si(001) substrate, fig. 3.21 (b) . . . . . . . . . . 49

3.24 3D non-contact AFM pictures of (a) as-deposited and (b) laser annealed Bi/In (45/45 nm) film on a $Si_3N_4$/Si(001) substrate. . . . . . . . . . . . . . 50
3.25 Contact AFM of 30/30 nm Bi/In as-deposited on glass: (a) AFM image (b) corresponding 3D image. . . . . . . . . . . . . . . . . . . . . . . . . . . 51
3.26 RBS spectra of Bi/In/Si(001) 120/120 nm thick samples, as-deposited (circles) and furnace annealed at 250°C (line). The arrows indicate the energy position of the element if it were at the surface. The shift in the Bi peak to lower energies with respect to the surface energy position, with the In peak being at the surface position indicates the presence of a thin (20 nm) surface In oxide layer in the as-deposited film. The degree of surface In oxidation increases after furnace annealing as seen by the surface oxygen peak and the increased shift in the Bi peak with no change in the In. . . . . . . . . . 53
3.27 RBS spectra from Bi/In/Si(001) 120/120 nm thick samples as-deposited (circles) and laser annealed (line), showing a large increase in oxygen content throughout the film and a reduction in the density. . . . . . . . . . . 54
3.28 RBS spectra showing the oxygen peak from Bi/In/Si(001) 120/120 nm thick samples as-deposited (circles), laser annealed (stars), and furnace annealed at 250°C (crosses). This shows that the oxidation in the laser annealed samples occurred throughout the film while that of the furnace annealed occurred only at the surface. . . . . . . . . . . . . . . . . . . . . . . . . 55
3.29 RBS spectra showing the Bi and In peaks from Bi/In/Si(001) 120/120 nm thick samples as-deposited (solid line), furnace annealed at 150°C (solid triangles) and 250°C (open squares). The lower energy tail is greatest for the 150°C furnace anneal indicating the film roughened further compared to the as-deposited and 250°C anneal. The shift in the Bi peak is greatest for the 250°C anneal which saw the greatest amount of surface oxidation. . 56

# Chapter 1

# Introduction

## 1.1 Motivation for this Work

A class of sputter-deposited, bimetallic thermal resists (BiIn, SnIn, BiSn) has been investigated by Glenn Chapman's group since 1999 [1] - [6]. These alloys, when exposed to laser light, change properties; including a change in structure, electrical properties, and transparency. The exposure energy required (7 mJ/cm$^2$) is comparable to the exposure energy of current organic photo-resists. In the case of Bi/In, prototype resists consist of stacked bismuth on indium layers (15 - 60 nm thick) with thickness ratios matching a eutectic alloy composition in the BiIn binary phase diagram.

The equilibrium phase diagram of Bi-In is shown in Figure 1.1 [7]. Besides In(Bi) and Bi(In) it shows four equilibrium binary phases BiIn and $BiIn_2$, $Bi_3In_5$, and $Bi_{0.06}In_{0.94}$ and three eutectic points at 345K (22 at % Bi), 362K (33 at % Bi), and 383K, (52.7 at % Bi). Based on this phase diagram we expect that the room temperature equilibrium condition for (50% composition) is a bilayer Bi/In film the alloy InBi. With heating InBi will melt at a very low temperature, 110°. Investigation by Chapman's group have determined that laser annealing in air or vacuum causes Bi/In films to become optically transparent. The motivation of this thesis work was to determine the nature of the transformations from an initially opaque metallic film to a transparent and conducting film. Was this an oxidation process or rather a metastable metallic alloy?

This thesis work used a combination of X-ray diffraction (XRD), transmission electron microscopy (TEM), Scanning Electron Microscopy (SEM) and Atomic Force Microscopy

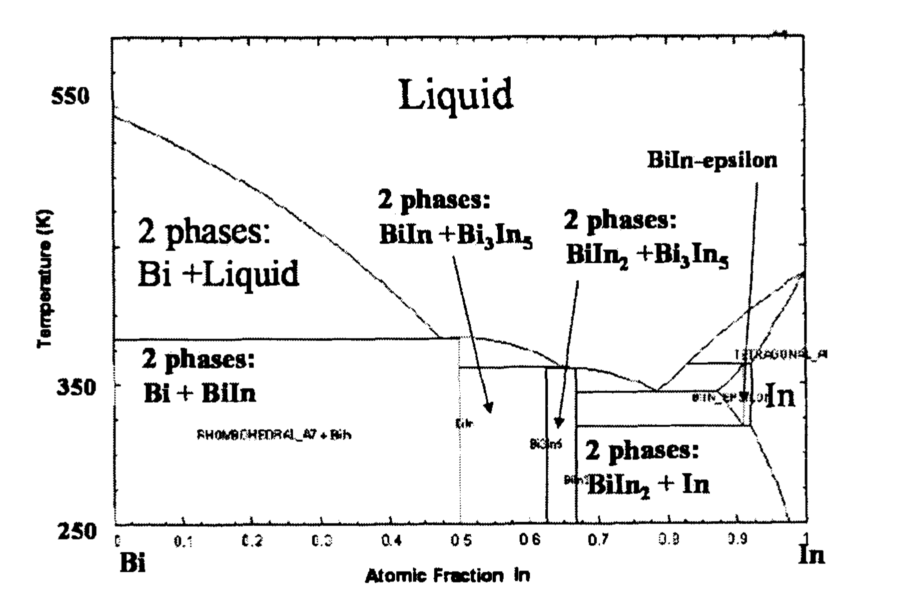


Figure 1.1: Bi-In phase diagram [7].

(AFM) to investigate the structure and morphology of the films before and after laser and furnace annealing. Hall effect measurements were used to investigate the electrical properties of the films after laser annealing.

## 1.2 Microlithography

Integrated circuit (IC) fabrication is a $222-billion industry worldwide [2]. The key to making IC's is the process of photolithography which transforms bare silicon wafers into functional microelectronic circuits found in everything from toasters to supercomputers.

Integrated circuits are built by the repeated process of creating thin layers of materials (like glass, or conductors) on the wafer surface, patterning those with photolithography, etching away unwanted portions of these films, then removing the materials used to make those patterns, as illustrated in Figure 1.2 [4]. These steps are repeated between 10 and 30 times in typical modern IC's.

### 1.2.1 Organic Photoresist

Current lithography uses photosensitive resists consisting of organic polymers that chemically change when exposed to light of a specific wavelength. Depending on the type of photoresist used, the interaction of the UV photons with the resist either increases or decreases the resist's solubility in a specific developer.

The patterned resist is subsequently used as a mask in an etching process. For example, if the substrate is being etched, it will only be attacked where the resist has been removed and the pattern is transferred from the resist to the substrate. The minimum feature size is the smallest line-width which can be reliably manufactured also called the critical dimension (CD).

Since organic photo-resists are very wavelength sensitive, new organic resists need to be created for each new wavelength as the exposure wavelength moves towards the Extreme Ultra Violet (EUV) to fabricate smaller transistors. As the exposure wavelength moves smaller, the photo-resists become increasingly more difficult to design. The higher absorption of smaller wavelength photons means that the resist absorb the exposed light at the surface of the resist instead of penetrating through the thickness to complete the exposure process. The energy of each photon exceeds the binding energy of the molecular bonds in the resist. It's large enough to damage many organic materials. Despite these challenges, organic based resists have continued to dominate micro-fabrication because they are extremely sensitive and have high resolution.

### 1.2.2 Inorganic Resists

Some research into next generation resists has shifted from organic to inorganic materials. There are advantages for such a change. One of these is that inorganic resists can be deposited by a number of dry processes, for example sputter deposition and Chemical Vapor Deposition (CVD), that are compatible with vacuum–based, all-dry lithography.

There are a number of inorganic compounds that are photosensitive and act in a similar manner to organic resists. For example, considerable study has been done on silver-based photoresist compounds such as $As_2S_3$ [3]. The silver-based resist scheme has the advantage of requiring a low exposure energy, on the order of (3 mJ/cm$^2$), which is only 30% of existing organic photoresist exposure requirements (10 mJ/cm$^2$). However, silver is a

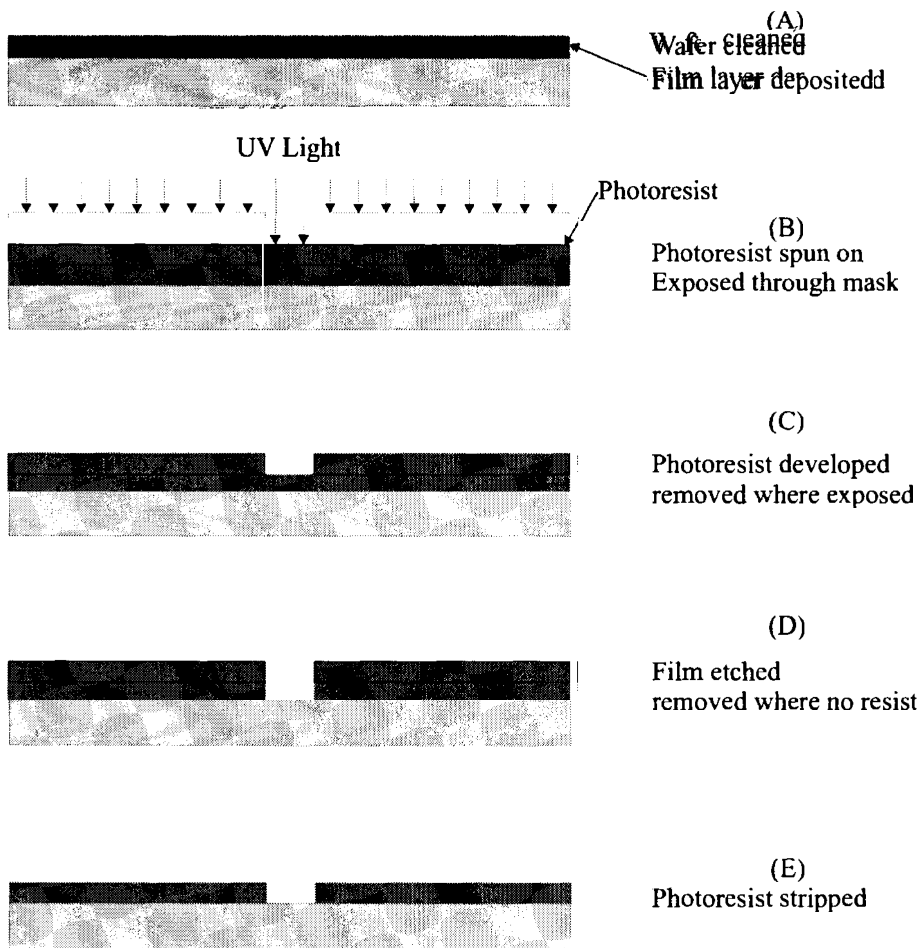


Figure 1.2: A simplified example of the microfabrication process, by permission, [5].

deadly poison to the Si transistor processes, diffusing rapidly through Si, kills carrier life-time making silver-based resist unusable [3].

Typical photo-resists are applied as a liquid, to drive out the solvents it will be baked in an oven for 20 minutes at 100°C [5]. Switching to an all-dry inorganic resist will eliminate organic materials in the process flow and reduce the number of cleaning steps that prevent contamination in the system. A fully dry fabrication would use only 0.01% of the material mass, 6% of the energy, and 62% of the time, a large saving in time, energy, and material. Much of these savings comes from the reductions in cleaning processes required by the organic resist [5].

The process developed by Chapman's group using a bimetallic thermal resist is shown in Figure 1.3 [5]. The metal layers, for example Bi/In, are sputter deposited at room temperature. UV or optical light is used to heat the layers forming an alloy that they observe becomes transparent.The exposure energy in these laser pulses creates sufficient heat that thermally activates the alloying process (300-800°C). Current microfabrication facilities use a 248 nm KrF excimer laser pulse to reliably create 0.18 micron structures. Unlike a photoresist, a phase transition happens in a thermal resist heating process. [1].

Two kinds of acid solutions were used to develop the resist by removing the unexposed area and retaining the exposed area 1.3(c). One is a nitric acid and acetic acid mixture (HNO3:CH3COOH:H2O=1:3:6) and the other is a dilute RCA2 solution (HCl:H2O2:H2O=1:1:48), all used at room temperature [8].

For a 45 nm / 45 nm Bi/In film, 100 seconds of development time were applied to ensure that all the scum (remnant material) was removed. The samples were N2–blown dried after the development and DI water rinse. Exposed resist can be stripped in a standard RCA2 (HCl:H2O2:H2O=1:1:6) at 80 °C within 10 sec.

## 1.3 Thesis Outline

Chapter 2 discusses the details of film formation and experiments performed to characterize BiIn thin films before and after annealing. Chapter 3 presents the results of crystallinity, morphology, and electrical properties. Chapter 4 concludes this thesis with a summary of the findings, comparison with Indium Tin Oxide (ITO), and a brief discussion of possible future work.

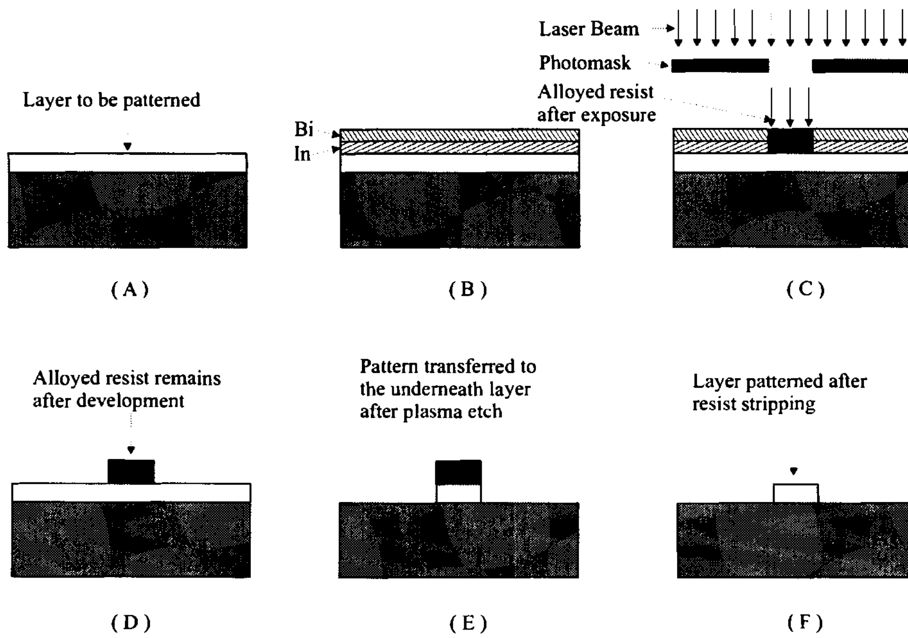


Figure 1.3: A dry bimetallic thermal resist process. (a) shows the substrate and the layer to be patterned. (b) In and Bi have been sputtered onto the substrate. (c) UV exposure converts the exposed area into an alloy, which has different chemical properties from the unexposed area. (d) The development process removes the unexposed and retains the exposed area. (e) The pattern is transferred to the underlying layer by either plasma or wet etch. (f) The whole process is completed by etching the exposed resist, by permission, [5].

# Chapter 2

# Experimental Procedures

## 2.1 Structural Properties

The crystal structure, surface morphology and electrical properties of the deposited film, before and after heating, were studied. This chapter will introduce and explain the theory of the techniques used for performing these studies. The discussion for each technique will contain three parts: a general overview of the theory and basic operation of the specific apparatus involved, the actual experiment, and finally the results.

## 2.2 Sample Preparation

### 2.2.1 Thin Films

Sputter deposition, and laser annealing of the thin film samples needed for the experiments were carried out in the Engineering Science microfabrication Laboratory at Simon Fraser University (SFU) by graduate student Yuqiang Tu and lab engineer Bill Woods. The Chapman group also used a profilometer to measure film thickness, a four-point probe to determine film conductivity, and a CARY 3EUV (extreme ultra violet) spectrometer to measure optical density. The electrical and optical measurements of this group will be summarized in related chapters.

Substrates used in the thin film experiments of this work were Si(100), and Si(111) wafers and glass slides. Wafers were plain or coated with $SiO_2$ and $Si_3N_4$, used to inves-

tigate the dependence of the substrate composition and structure on film properties. The Bi/In bimetallic films were DC-sputter-deposited using a Corona machine that can deposit multi-layers. The targets used were two-inch in diameter 99.99% Bi and 99.99% In. Before sputtering, the sample substrates were cleaned, using standard processes (RCA1 and RCA2) [6], then baked for 20 minutes at 120°C to remove moisture. After loading the samples into the vacuum chamber, it was pumped down to a base pressure of $6 \times 10^{-7}$ Torr. During sputtering, the chamber pressure was maintained at 4 mTorr by using Ar gas flowing at 10 sccm [8]. Bi and In deposition rates were about 1.2 and 0.4 nm/Wmin, respectively.

A majority of the samples prepared were 45/45 nm 1:1 Bi/In thin films on either glass or silicon substrates. Each of the above sample types were analyzed by XRD, SEM, AFM and Hall effect measurements. Additionally, thinner 12/12 nm 1:1 Bi/In thin films on Si(111) and SiO and C-coated Cu grids were fabricated and analyzed by XRD and TEM measurements. A list of samples including the thickness, date deposited, and analysis carried out is found in Table 2.1.

Bismuth has the lowest thermal conductivity of all metals with the exception of mercury [29]. The reflectivity of bismuth is about 32% at the wavelengths of interest [9]. These characteristics of Bi make it a preferred metal for the top layer of a bilayer film. Both bismuth and indium have a low eutectic T. Other physical and chemical properties of bismuth and indium are listed in Table 2.2 [10], [11].

To give better control of film thickness, a different RF power is used for Bi and In sputtering, since the In sputter rate is lower than that of Bi. To prepare a Bi/In film the DC voltage is 350V, 500V and the current is 0.7A, 0.2A for In and Bi, respectively [8]. This gives DC sputter powers of 245 W and 100 W ($P = IV$, $245 = 350 \times 0.7, 100 = 500 \times 0.2$), respectively. The atomic ratio of equal thickness of thin film Bi to In is about 1:1, smaller than for bulk material [6].

Bi/In films were laser annealed or furnace annealed. For laser exposure, they were scanned for 30 min. with 0.9W with an Argon laser beam ($\lambda$ = 488 - 514 nm), focused with a 50× objective lens. The films can be masked by a patterned metal plate laid directly on the surface. Unexposed regions of the BiIn structure can be removed by immersing in acid solutions. Either a nitric and acetic acid mixture ($HNO_3$:$CH_3COOH$:$H_2O$=1:3:6), or dilute RCA2 solution ($HCl$:$H_2O_2$:$H_2O$=1:1:48) is used at room temperature [8]. For a 45 nm /45 nm Bi/In film, 100 seconds of development time is optimal for ensuring complete removal

Table 2.1: List of sputtered-deposited samples investigated.

| sample | Heating Process | Substrates | Thickness $\pm$ 1 nm | Fab.Date | Measurements |
|---|---|---|---|---|---|
| A | Laser-annealed 0.9 W | Si(001) | 12/12 | 10/25/02 | STEM, TEM XRD, AFM SEM |
| B | Laser-annealed 2.5, 3,2 W | Si(001) | 12/12 | 02/20/03 | XRD |
| C | Laser-annealed 0.9 W | Si(001) Si(111) $Si_3N_4$/Si(001) $SiO_2$/Si(001) Glass | 45/45 | 02/15/03 | XRD,SEM AFM, Hall |
| D | laser-annealed 0.9 W | Si(001) | 120/120 | 05/15/02 | RBS, XRD SEM, AFM |
| E | Laser-annealed 0.9 W | Si(111) | 45/45 | 06/25/03 | XRD |
| F | laser-annealed 0.9 W | Glass | 90/90 | 06/21/01 | XRD |
| G | Furnace-annealed 150, 200, 250°C | SiO and C coated Cu grids | 12/12 | 06/13/02 | TEM |
| H | bulk alloying | | | 08 /10/02 | XRD |

of the layers, while minimizing etch damage of the substrate.

A group of samples were also prepared on grids for TEM measurements (group G). After sputter-deposition on grids they were annealed in a furnace. Furnace anneals were carried out in an oven at temperatures of 150°C, 200°C, and 246°C, for 5 hours and then cooled slowly.

Table 2.2: Properties of bismuth and indium [10, 11].

| | Bismuth (Bi) | Indium (In) |
|---|---|---|
| Physical State | Solid | Solid |
| Appearance and Odor | Gray, soft, bright metallic luster powder and pieces | Soft silvery white metal odorless |
| Crystal structure | Monoclinic | Tetragonal |
| Atomic Mass | 208.98 | 114.82 |
| Vapor Pressure | 1 mm at 1020 °C | 27 atm at T melt |
| Solubility in $H_2O$ | insoluble | insoluble |
| Density (kg/m$^3$ ) | 9780 | 7310 |
| Boiling Point °C | 1420 | 2000 |
| Melting Point °C | 271.3 | 157 |
| Electrical Resistivity ($\mu\Omega$ cm) | 130 | 11 |

### 2.2.2 Bulk BiIn Alloys

We also prepared bulk 50% (1:1 atomic ratio) Bi/In alloys under controlled conditions. In an oxygen-free environment, BiIn alloy forms and melts at approximately 110 °C [12]. Oxidization occurs at room temprature, but is kinetically limited to a thin surface layer. Preparation was done in the chemical preparation room (P8400) in the physics department in a glove box filled with purified $N_2$.

Indium pieces were soaked in HF: $H_2O$ (1:4) for 1 minute to obtain an oxide free surface. In a $N_2$ environment a hot plate was used to heat the Bi (melting at 271.3°C) in a Pyrex beaker on a hot plate at more than 270°C until it started melting. Then, the In was added, and the mixture was heated, until all of the In also melted. After another 15 minutes of heating in the same range of temperature, the hot plate was turned off, and the beaker was left to cool for several hours. A similar run was carried out with same weight percentage of each metal. After the metals melted they were stirred continuously with a glass rod, then the beaker was left overnight to cool in air outside the glove box.

## 2.3 Principles of X-Ray Diffraction

Around 1911 Bragg, von Laue, Darwin, and Ewald developed an X-ray diffraction (XRD) theory to explain the non-specular reflection and transmission of X-rays in crystalline material, through properties of wave interference. It was later in the early 1980's that a great push in the advancement of X-ray diffraction resolution was made to address the needs of the emerging semiconductor industry [13].

X-ray diffraction is one of the most important characterization tools used in solid state chemistry and materials science. Each crystalline solid has its unique characteristic X-ray diffraction pattern, a "fingerprint" used for its identification [16].

Diffraction occurs when radiation, with wavelength $\lambda$, is incident on a crystal with lattice spacing, d, such that the angle of incidence, $\theta$, satisfies the condition of Bragg's law, defined in 1912 by W. L. Bragg as follows:

$$n\lambda = 2d\sin(\theta). \tag{2.1}$$

This relationship describes constructive interference by the incident and reflected rays for n = an integer, 1, 2, 3,.... multiple periods.

The peaks in an X-ray diffraction pattern are directly related to the atomic distances for each planar spacing. We could determine the size and the shape of the unit cell for any compound. Powder diffraction pattern methods were established for the study of polycrystalline metals and alloys.

The setup for a typical X-ray diffraction experiment is shown in Figure 2.1 [16]. Incident and diffracted beams lie in a plane which also contains the sample normal. If the angle of the sample surface is $\theta$ with respect to the incident beam, the angle of the diffracted beam is $2\theta$ with respect to the incident beam.

We studied the structural properties of samples A, B, C, F and G, using the Norelco Diffractometer (Model 3-202). The Norelco Diffractometer is located in the physics department, Shrum Science Center, Room P8412 at Simon Fraser University (SFU). The X-ray source was a copper sealed tube with 2 characteristic wavelengths at $K_{\alpha_1}$ and $K_{\alpha_2}$ ($\lambda_1$= 1.5406 $\AA$, $\lambda_2$ =1.54434) powered by a Philips PW 1730 X-ray generator. The slit define a beam of width of 0.5 degrees comparable to the instrument resolution. The sample was placed face side up with respect to the beam. An XRD spectrum was obtained over a $2\theta$

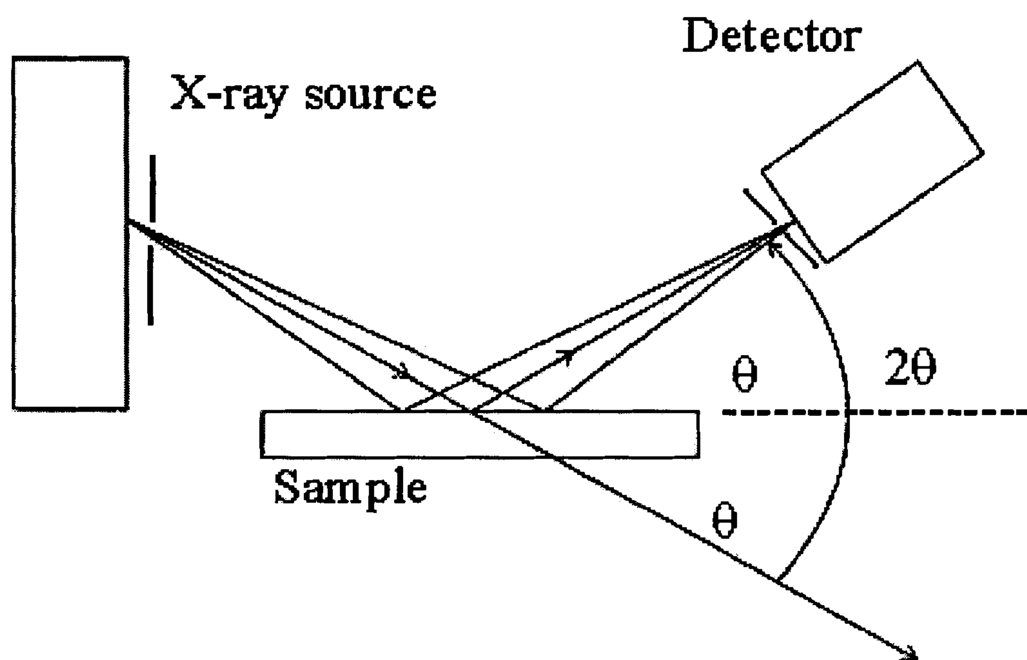


Figure 2.1: Schematic of an X-ray powder diffractometer, by permission [16].

range of 10 - 80 degrees, with a step size of 0.05 degrees, counting 1 second per step, or 10 seconds per step for the sake of increasing signal to noise.

The analysis was based on brag's law Eq. and calculation of d-spacing and comparing the results with the latest reported database of inorganic materials (JCPDS-ICDD Copyright (c) 1993)).

## 2.4 TEM (Transmission Electron Microscopy)

The Transmission Electron Microscope was developed in the 1930's to achieve higher resolution than is available by optical and UV diffracted limited imaging techniques. For example, green light with a wavelength of 0.5 $\mu$m has a theoretical image resolution of about 0.2 $\mu$m. By comparison the resolution of a TEM is 1-3 Å depending on the acceleration voltage (200 keV) and objective lens quality. TEM is a complementary tool to conventional crystallographic methods such as X-ray diffraction [18].

The main structure of a TEM is an evacuated metal cylinder (the column) about 2 meters high. A filament at one end of the when heated emits electrons due to heating. The emitted electrons are accelerated by an anode held at a 200,000 Volt potential with respect to the filament (cathode). They travel down the column and are focussed by electromagnetic lenses on to the sample [18].

### 2.4.1 Modes of Operation

**Classic TEM.**

Transmission electron microscopy involves the diffraction of electrons in crystalline materials and analysis of the scattering and diffracted beam as a means to probe material structure. In these studies there are several modes of operation including: Dark–Field (DF), Bright–Field (BF) and Selected Area Diffraction Pattern (SAD) [15]. BF imaging is based on mass or diffraction contrast. The DF mode images specific regions or phases in the sample diffracting into chosen beams. SAD is a mode that makes it possible to view and record the electron diffraction pattern from areas as small as $\sim 1\mu$m [18].

The Hitachi 8100 TEM in room P8426 at Simon Fraser University (SFU) was used to obtain Bright Field, Dark Field, and SAD images at 200 keV. The starting vacuum pressure

was $3\times10^{-7}$ Torr, and it remained less than $5\times10^{-7}$ Torr throughout the duration of the experiment. The magnification used in obtaining the Bright and Dark Field images was commonly 100 kX. The camera length used for the SAD image was 0.8 m. Fresnel fringes at sample edges were observed first, and were accordingly used as a means to focus the images.

### 2.4.2 Scanning TEM (STEM)

Field-emission Scanning Transmission Electron Microscope (STEM) with a high angle annular detector (HAADF) was also used. HAADF imaging gives intensity strongly correlated to the atomic number, that is z contrast.

The HAADF detector consists of a scintillator-photomultiplier with single-electron sensitivity. [18] In the STEM, images are acquired by moving a focused beam of electrons in a raster across the specimen and collecting the transmitted electrons at each x,y pixel coordinate. The electron probe size can be as small as 1 Å. The analysis of our samples was done at Simon Fraser University with the Tecnai F20 that is located in the chemistry department, Room C6018.

### 2.4.3 Sample Thinning for TEM

Specimens that are examined in TEM need to be electron transparent. In the case of InBi alloys they need to be less than few tens of nanometers (about 30 nm) to be electron transparent. We employed three methods for generating thin samples. In our first method, we removed the thin film layer from a glass substrate by dissolution of the substrates in hydrofluoric acid. Our second, and more successful method involved deposition of thin films directly on TEM grids. Finally, we also generated some thin film samples by mechanical polishing and ion milling of a silicon substrate.

Samples of 15 nm /15 nm Bi/In film deposited on glass slides were etched in 50% HF (mixed with distilled water). The sample was left in the etchant for 30 sec. The glass was etched by the solution at the edges, and underneath the film, and pieces of film came off. Folding copper grids were used to support and pick up the pieces of broken film. We rinsed the film in acetone, since water would break the films because of surface tension.

Carbon formvar support films on Cu grids have very low mass and were used as substrates for sputtering of 12 nm/12 nm Bi/In films for TEM. SiO support films were also chosen because they simulate glass and silicon substrates.

Thinning by ion milling or chemical etching, requires mechanical polishing as the first stage in the specimen preparation process. We used a thermoplastic wax to hold the sample, thin film side down, onto a stainless steel cylinder, and polished it down to 30 - 120 microns from the back. Initially, we used SiC (silicon carbide) paper, lubricated with water for grinding. We ground the sample using a series of progressively finer grit, each stage removing the damage inflicted on the sample by the previous stage. At the last stage, we used alumina, $Al_2O_3$, powder suspended in water for final polishing of the samples. The final polishing is performed slowly to make sure that the sample is not polished away completely.

The thickness of the sample is measured frequently using a stylus, especially when the thickness of the sample is close to the desired value. To avoid applying excess pressure on the thin sample, the thickness measurement is taken from the wax border surrounding the sample. The samples are removed from the polishing cylinder by melting the wax or dissolving it in acetone.

In an ion mill, a sample is bombarded by a focussed beam of high energy ions. We used a "Gatan Dualmill" Ar ion mill to completely penetrate the Si substrate. A gun voltage of 5.5 kV, current of 30 $\mu$A, and vacuum pressure of $3 \times 10^{-5}$ Torr was used. The ion beam was directed at the back of the sample at a 18°C incident angle. The milling is stopped upon first detection of the through hole, apparent by the increased brightness of light passing through the sample. The rate of removal varies with beam energy and incidence angle. The rate is typically a few microns per hour. Ion milling of the 30 $\mu$m thinned samples took about 2-8 hours. Therefore, the rate of removal is estimated to be 7.5 $\mu$m per hour. The shape of the hole perimeter is a gently sloped wedge providing sample area for TEM analysis.

We attempted to pre-thin the substrate before depositing the BiIn. Holes were generated in mechanically thinned substrates by a simple lithographic technique utilizing paraffin wax masks and acidic etchant. Samples processed in this way are unique in that the BiIn films were grown after the thinning of the substrate was complete.

An n-type (100) silicon was chosen for this purpose and it was mechanically polished down to 120 microns from the back. Then the polished silicon was broken into 2 mm pieces. Paraffin wax was used to cover the surface of the substrate. The wax film was

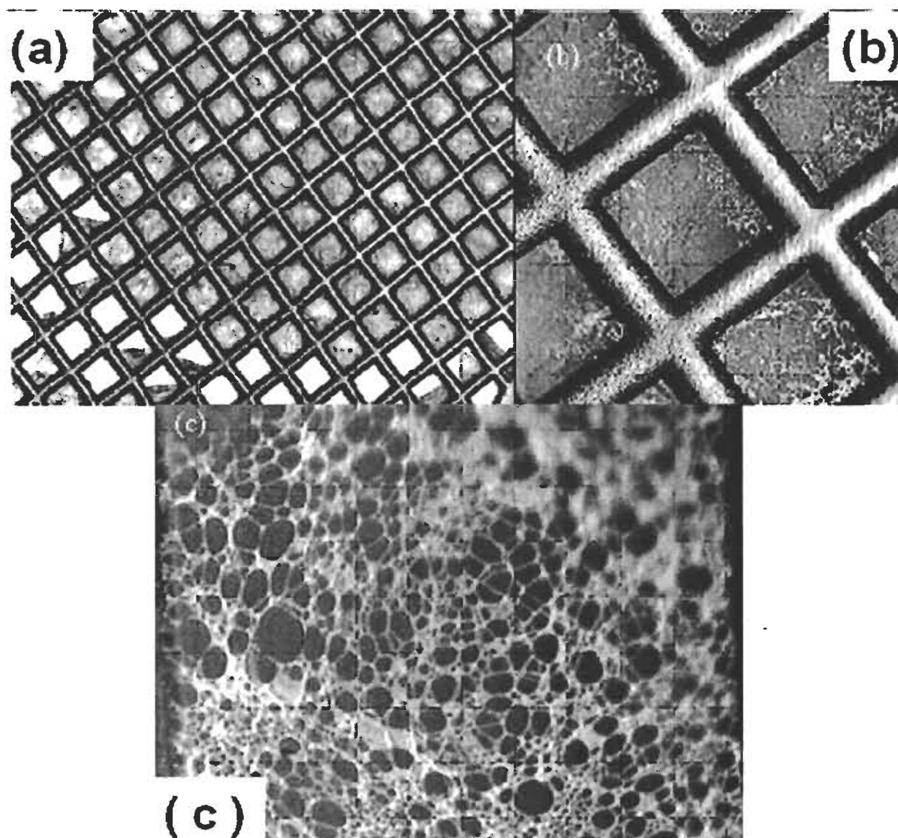


Figure 2.2: Optical photographs of increasing magnification of 12/12 nm BiIn as deposited on 300 mesh, lacy carbon support grid ($10\times10$ $\mu$m grid size). In some regions the lacy carbon is interconnected by the film but mainly there is no film left across the holes.

punctured with a pin, to create a small exposed region of the substrate. The substrate was then immersed in an acid mixture (HF: $HNO_3$ = 4:5) in a well illuminated glass container under an optical microscope. After about 12 minutes, light was observed to go through the silicon piece where a hole was created in the paraffin. In the early attempts, acid mixtures "$CH_3COOH$: HF: $HNO_3$ = 6:3:5" and "$CH_3COOH$: HF: $HNO_3$ = 1:3:5" were used, but nothing happened after waiting for 45 and then 20 minutes, respectively. Therefore, acetic acid was eliminated in the solution and hydrofluoric acid was increased to make the solution stronger. Bi/In was then sputtered on the front side of the etched silicon.

## 2.5 Surface morphology

To investigate the surface morphology of the BiIn films we used Scanning Electron Microscopy (SEM) and Atomic Force Microscopy (AFM). Principles of SEM and AFM instrument operation are the subject of this section.

### 2.5.1 Scanning Electron Microscopy (SEM)

Scanning electron microscopy (SEM) is primarily used to study the surface structure of materials. SEM employs a focussed beam of energetic electrons (e.g. 5-30 keV), imaging materials with a resolution of 3 nm. The main structure of a SEM includes the electron gun, condenser lenses, and vacuum system ( $< 1.0^{-5}$ mbar) [19]. The Free Working Distance (FWD), the distance between the sample surface and the bottom of the electron column, is less than 7 mm.

The FEI (Strata DB 235M) SEM in the Shrum Science Center, Room P8414 at Simon Fraser University was used to image the BiIn samples. The beam of electrons in a SEM is to be directed at the specimen but not to charge up the specimen. Therefore, the surface of the sample should be electrically grounded to the stage. Surfaces comprised of insulators and poor conductors may be coated with carbon or gold. Since the BiIn films are conductive, no coating was required. However, since the silicon substrates of our samples are relatively poor conductors, carbon paint was used to make an electrical connection between the conducting film and the sample holder.

### 2.5.2 Atomic Force Microscopy (AFM)

Atomic Force Microscopy (AFM) is a Scanning Probe Microscopy (SPM) technique which utilizes a low spring constant cantilever with a very sharp tip of a few nanometers in diameter (1 nm to 10 nm in radius). As the probe is scanned over a surface, the degree of its deflection varies in response to variations in the surface's topology. From records of the probe deflection as a function of lateral position over the sample surface, a three-dimensional image of the surface topology can be obtained with a lateral resolution of 1-2 nm and a vertical resolution of 0.01 nm. AFM provides measurements of surface roughness.

Two modes of operation are possible: contact and non-contact. In contact AFM, the

tip makes soft physical contact with the sample. In the non-contact AFM, the cantilever is vibrated near the surface (1-10 nm above the surface). In both modes, van der Waals forces cause the cantilever to bend in response to changes in the surface topography, as the tip is scanned over the surface [20].

Typical AFM cantilever spring constants are between 0.001 to 100 N/m, and deflections from microns to 0.1Å can be measured. Typical forces between tip and sample range from $10^{-11}$ to $10^{-6}$ N. For comparison, the interaction between two covalently bonded atoms is of the order of $10^{-9}$ N at separations of 1Å. Therefore, non-destructive imaging is possible with these small forces

Examination of the BiIn film surface on the nanometer scale is possible. Sample's analyzed by AFM are held by double sided tape on the AFM sample holder. The surface of the film must not be too rough, otherwise, the AFM tip will break. Also, if the film is too soft, the AFM tip may scratch or stick to the surface resulting in a noisy AFM trace.

The surface topography of some of the samples was studied using the Explorer non-contact AFM, manufactured by Thermo Microscopes. This AFM is located in the chemistry department, Room C8036 at Simon Fraser University (SFU). Most images were obtained using a Parc Scientific non-contact AFM in the physics department in Dr. Simon Watkin's lab. The non-contact mode imaging was done in Dr. Gary W. Leach's lab in chemistry department at Simon Fraser University.

## 2.6 Material Composition

### 2.6.1 Rutherford Backscattering Spectrometry

Rutherford backscattering (RBS) is a standard technique in the analysis of materials used to determine the elements that are present in a given sample. This technique is fully quantitative and the use of external standards is not necessary [21]. Computerized interpretation of RBS data has been common practice for over two decades and several programs have been developed to facilitate the task of data analysis [23].

Typically RBS is used not only to determine thin film thickness and composition as a function of depth, but also to determine lattice disorder and location of lattice impurities [23]. We exploited this technique for determining composition of our samples.

In the RBS spectrometer, the analyzed sample is bombarded by high energy helium ions. The yield and energy of the elastically back scattered ions depends on the sample composition. Analysis of our samples by RBS was carried out at the Dept. of Physics, University of Western Ontario, London. The RBS operating conditions were: 2.3 MeV beam energy, 10-100 nA He+, and a 1 $mm^2$ beam spot.

The concentration of oxygen in the sample was measured using nuclear reaction analysis (NRA). At a beam energy of 3.03 MeV $He^{++}$ reacts with oxygen nuclei with an enhanced probability giving a high sensitivity.

## 2.7 Electrical Properties

### 2.7.1 Hall Measurements

Discovered by E. H. Hall in 1879, the Hall effect is a technique for determining resistivity, mobility, and free carrier concentration in semiconductor materials [24].

The standard geometry used for Hall measurements is based on the Hall bar as depicted in Fig. 2.3. A bar of width w and thickness d contains n carriers of charge q. An electric field $E_{BD}$ is applied in the BD-direction of the bar and magnetic field is applied perpendicular to $E_{BD}$. The resultant force on the free carriers is given by the Lorentz law:

$$F = q(E + \nu \times B), \tag{2.2}$$

where $\nu$ = the velocity of the carriers. The results are measurement of carriers plus potential $V_{AC}$. In steady state the magnetic force is equal to the electric force across the bar:

$$qE_{AC} = qvB. \tag{2.3}$$

The resulting Hall voltage $V_{AC}$ is given by:

$$V_{AC} = E_{AC}w = v_{BD}Bw. \tag{2.4}$$

Equivalently,

$$V_{AC} = \frac{I_{BD}}{qnwd}Bw = \frac{1}{qn}\frac{I_{BD}B}{d} = R_H\frac{I_{BD}B}{d}. \tag{2.5}$$

where we have substituted the following for $v_{BD}$:

$$j_{BD} = \frac{I_{BD}}{wd} = qn\langle v_{BD}\rangle. \tag{2.6}$$

Furthermore, we introduced the hall coefficient, $R_H$:

$$R_H = \frac{1}{qn} = \frac{dV_{AC}}{I_{BD}B}. \tag{2.7}$$

Measuring the Hall Mobility $\mu_H$, the Hall voltage, and resistivity, ρ, can be calculated:

$$\rho = \frac{Rwd}{L} = \frac{V_{BD}wd}{I_{BD}L}. \tag{2.8}$$

$$\mu_H = \frac{R_H}{\rho}. \tag{2.9}$$

### 2.7.2 van der Pauw Theory

Hall bars can present difficulty in thin film semiconductors, as producing this shape requires fabrication involving lithography and etching steps [13]. The van der Pauw method [24] allows for Hall measurements to be done on arbitrary, flat-shaped samples removing the difficulty and time in fabricating Hall bars. Also, it is not necessary to have precise measurements of the lateral sample dimensions, as only thickness measurements are required. The typical geometry of a van der Pauw sample is depicted in Figure 2.3 and can be completely arbitrary as long as the above mentioned conditions are satisfied. The resistance is the potential difference between two adjacent points (C, D) when the applied current is flowing between two other adjacent points (A, B):

$$R_{AB,CD} = \frac{V_C - V_D}{I_{AB}}. \tag{2.10}$$

The corresponding resistance, $R_{BC,DA}$, is similarly defined:

$$R_{BC,DA} = \frac{V_A - V_D}{I_{BC}}. \tag{2.11}$$

From boundary conditions it was shown by van der Pauw that the following expression holds [24]:

$$\exp\left(\frac{-\pi R_{AB,CD}d}{\rho}\right) + \exp\left(\frac{-\pi R_{BC,DA}d}{\rho}\right) = 1. \tag{2.12}$$

For a sample with four fold symmetry it can be assumed that $R_{AB,CD} = R_{BC,DA}$, so for a symmetric sample $\rho$ can be calculated with the following formula [24]:

$$\rho = \frac{\pi d}{\ln 2} \frac{R_{AB,CD} + R_{BC,DA}}{2}. \tag{2.13}$$

This equation is further improved by expanding the averages of $R_{AB,CD}$ and $R_{BC,DA}$ to also include $R_{CD,AB}$ and $R_{DA,BC}$. When the sample is asymmetric the resistances will differ from each other. In this case an additional correction factor to $\rho$ is applied as shown by van der Pauw [24]. If a magnetic field is applied perpendicular to the sample as shown in Figure 2.3, the potential difference will be changed, and the Hall coefficient is calculated with the following relation [24]:

$$R_H = \frac{d}{B} \frac{\Delta(V_A - V_C)}{I_{BD}} = \frac{d}{B} \frac{(V_A' - V_C') - (V_A - V_C)}{I_{BD}} = \frac{d}{B}(R'_{BD,AC} - R'_{BD,AC}). \tag{2.14}$$

The Hall mobility is then given by:

$$\mu_H = \frac{R_H}{\rho} = \frac{d}{B}\left(\frac{R'_{BD,AC} - R_{BD,AC}}{\rho}\right) = \frac{2\ln 2}{\pi B}\left(\frac{R'_{BD,AC-BD,AC}}{R_{AB,CD} + R_{BC,DA}}\right). \tag{2.15}$$

### 2.7.3 Experimental Hall Setup

The van der Pauw technique was used to obtain all Hall measurements of carrier concentration and mobility of the Bismuth Indium films in this work. A magnetic field of 0.5 Tesla was used in a Hall system in Dr. Simon Watkin's lab at SFU. Indium was used to make electrical contacts. In most practical ohmic contacts to semiconductors, the metal layers usually contain a suitable dopant species - donor or acceptor atoms. Heat treatment in a hydrogen atmosphere is used to drive the dopant into the semiconductor to form a $n^{++}$ or $p^{++}$ layer thus creating a tunneling metal-semiconductor junction required for enhanced ohmic behavior. The temperature range for this process is typically 250 °C to 300 °C [24]. Since our samples are sensitive to heat we couldn't follow the regular process of contact formation. Instead we formed contacts by manually pressing sub-millimeter indium wires onto the sample surface. We prepared our samples prior to contact formation by dipping them in 10% HF solution followed by a DI water rinse.

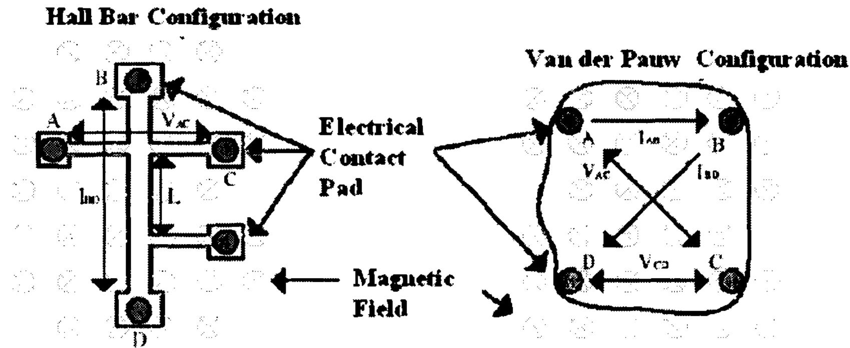


Figure 2.3: Hall bar and van der Pauw sample schematics. In both schematics the current $I_{BD}$ and a magnetic field B produces a Hall voltage $V_{AC}$. From a measurement of the Hall voltage ($V_{AC}$) for a known current ($I_{BD}$) and magnetic field (B) the net carrier concentration can be determined, by permission, [13].

### 2.7.4 Four–Point Probe

Four Point Probe was used to find the resistivity (ρ) and sheet resistance (R) is as follows [14]:

$$R = \int_{x_1}^{x_2} \rho \frac{dx}{2\pi x t} = \int_{s}^{2s} \frac{\rho}{2\pi t}\frac{dx}{x} + \frac{\rho}{2\pi t}\ln(x)|_s^{2s} = \frac{\rho}{2\pi t}\ln 2. \tag{2.16}$$

where t=film thickness and $R = \frac{V}{2I}$ , the sheet resistance for a thin sheet is:

$$\rho = \frac{\pi t}{\ln 2}(\frac{V}{I}). \tag{2.17}$$

Yuqiang Tu, Ph.D. student of Dr. Chapman, measured the sheet resistance of the exposed and unexposed samples using a MP0705A (Wentworth Lab) four-point probe connected to an HP 3478A multimeter.

# Chapter 3

# Results and Discussion

## 3.1 Structural Properties

### 3.1.1 XRD Results – Thin Films

XRD scans show that two layer Bi/In thin films convert to a bismuth indium alloy during the deposition process. After annealing BiIn alloy converts to oxide forms of bismuth and indium with a random orientation in all samples, regardless of the substrate orientation. Fig 3.1 shows the XRD scans from two of the thinnest samples, 12/12 nm, both deposited on Si(001). Figure 3.1 (a) is sample A (Table 2.1) as-deposited, and (b) is laser-annealed at 0.9 W. Fig. 3.1 is sample B (Table 2.1), as-deposited (i) and laser annealed in air at 2 higher laser powers, (ii) 2.5 and (iii) 3.2 W. The range of the heat that these samples received is about 300-500°C. It is clear that the as-deposited films have already alloyed forming BiIn, $BiIn_2$ and $Bi_3In_5$ binary alloys. Although the thickness of these films was nominally the same, there is an obvious difference in the intensity of the peaks observed. In the case of sample B there is a strong preferred orientation(001). After laser annealing oxides formed.

With increasing laser power, stronger bismuth oxide peaks are observed with fewer indium oxide peaks. Comparing Fig 3.1 (a) to Fig 3.1 (b) we see that there are more oxide peaks present for the sample laser annealed at lower power. It is possible that the crystalline structure of the more heated film is increasingly amorphous at greater laser powers, or that the In is evaporating. Since it is not easy to combine Bi and oxygen as a stable bond, there is possibility of amorphous Bi forming, or if in case of Bi-O bond is an strong bond so we

have more Bismuth oxide forming than indium oxide.

Similar results are found for thicker films. Shown in Fig. 3.2 and Fig. 3.3 are the XRD scans from as-deposited and laser-annealed 45/45 nm films (samples C Table 2.1) as a function of substrate type.

These films were deposited simultaneously on Si(111), Si(100), $Si_3N_4$/Si(001), $SiO_2$/Si(001), and glass. No unalloyed Bi or In remained in the as-deposited films. Although they are the same thickness, there is a variation in the intensity of each peak. In all cases BiIn and $BiIn_2$ have formed but sometimes there is a pronounced preferred orientation in the film (e.g. Fig 3.2) (c). After laser annealing, the intensity of the oxide peaks for the Si wafer films are almost identical, whilst the glass sample is significantly different. The same oxide phases $In_2O_3$ (Cubic file number 6-416, and Rhombohedral (Hexagonal) file number22-236,(JCPDS-ICDD Copyright (c) 1993)) and bismuth oxides ($Bi_2O_3$, $Bi_2O_{2.33}$, δ-$Bi_2O_3$, BiO) are present but there is an increase in the number of peaks attributed to indium oxides compared to bismuth oxides.

The XRD results from 90, 180, 240 nm thick films on Si and glass substrate are shown in Fig. 3.4 and Fig. 3.5, as-deposited and laser-annealed, respectively. There is also a variability in the peaks observed for both as-deposited and after laser annealing. Again the films completely oxidize.

As a summary for XRD measurements on this films we can conclude that the films already alloyed forming predominantly BiIn during the sputter deposition process. They are polycrystalline in both as-deposited films and after annealing. Orientation of the film is totally random independent of the substrate, except for two cases that were not reproduced. The behavior did not depend on the film thickness up to 120/120 nm. The films oxidize after annealing into Bi and In oxides including $In_2O_3$ (cubic and rhombohedral), $Bi_2O_3$, β-$Bi_2O_3$, δ- $Bi_2O_3$, $Bi_2O_{2.33}$ and BiO. You can see more details about orientation in tables in appendix A (A.1- A.7).

### 3.1.2 XRD Results – Bulk Alloy

Results from XRD are shown in figure 3.6. The spectrum (a) is from the sample formed by melting Bi and In solid metals together, heating to 270°C and cooling in a $N_2$ environment. We see predominantly the BiIn alloy as expected from the equilibrium phase diagram. For

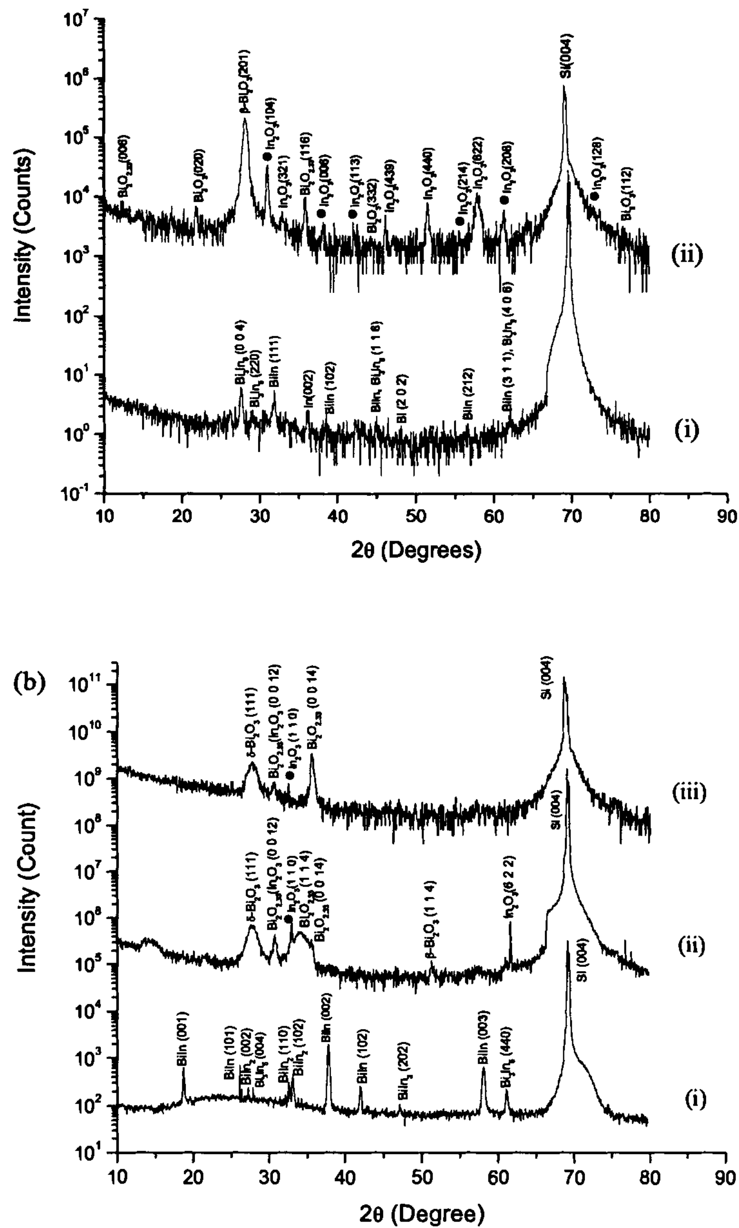


Figure 3.1: (a) XRD scans of (i) as deposited (ii) laser annealed (0.9W) Bi/In (12/12 nm) films on Si(001) (sample A, Table 2.1). (b) XRD scans of (12/12 nm) Bi/In films on Si (001), (i) as-deposited, and laser annealed in air with (ii) 2.5 W and (iii) 3.2 W power (sample B, Table2.1). The marked (•) indium oxide is referring to the rhombohedral structure of this alloy and unmarked one is refereing to the cubic structure.

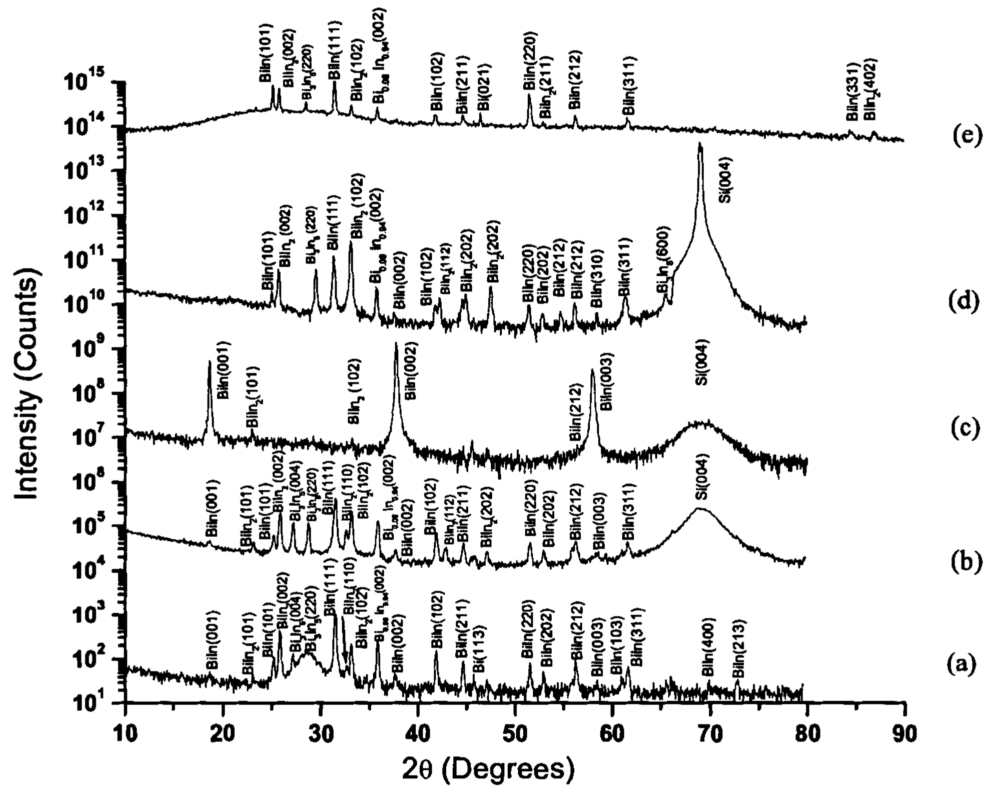


Figure 3.2: XRD scans of as-deposited Bi/In (45/45 nm) films on (a) Si(111) (b) Si(001), (c) $Si_3N_4$/ Si(001), (d) $SiO_2$/ Si(001), and (e) glass, substrates.

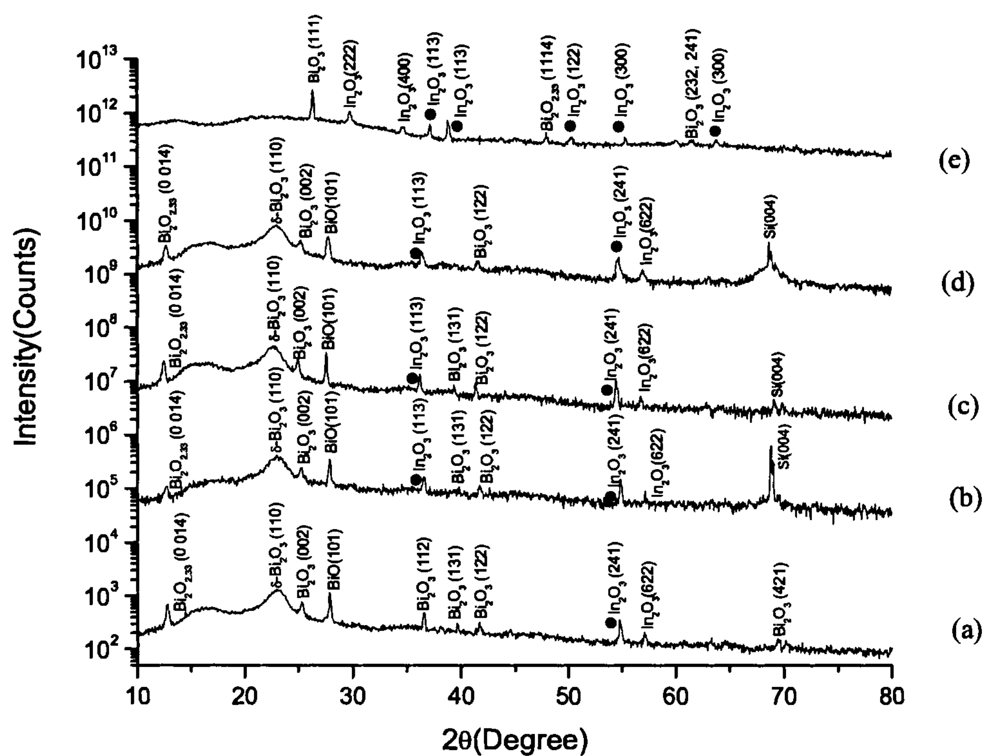

Figure 3.3: XRD scans from laser annealed of 45/45 nm Bi/In film of Fig. 3.2 on (a) Si(111) (b) Si(001), (c) $Si_3N_4$/ Si(001), (d) $SiO_2$/ Si(001), and (e) glass substrates (sample C, Table 2.1). This figure shows the same structural formation after annealing for the Si substrates but glass is different. The marked (•) indium oxide refers to the rhombohedral structure of this alloy and unmarked one refers to the cubic structure.

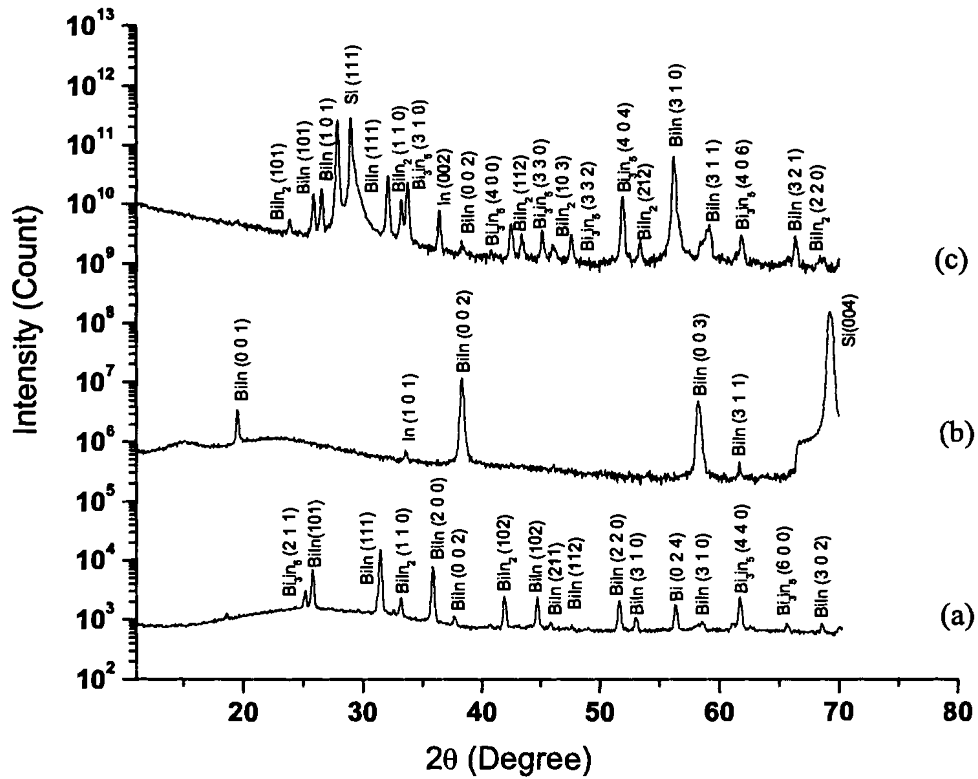


Figure 3.4: XRD scans from as-deposited Bi/In film deposited on (a) glass 90/90 nm, (b) Si (001) 120/120 nm, and (c) Si (111) 45/45 nm (samples D, E, F in Table 2.1)

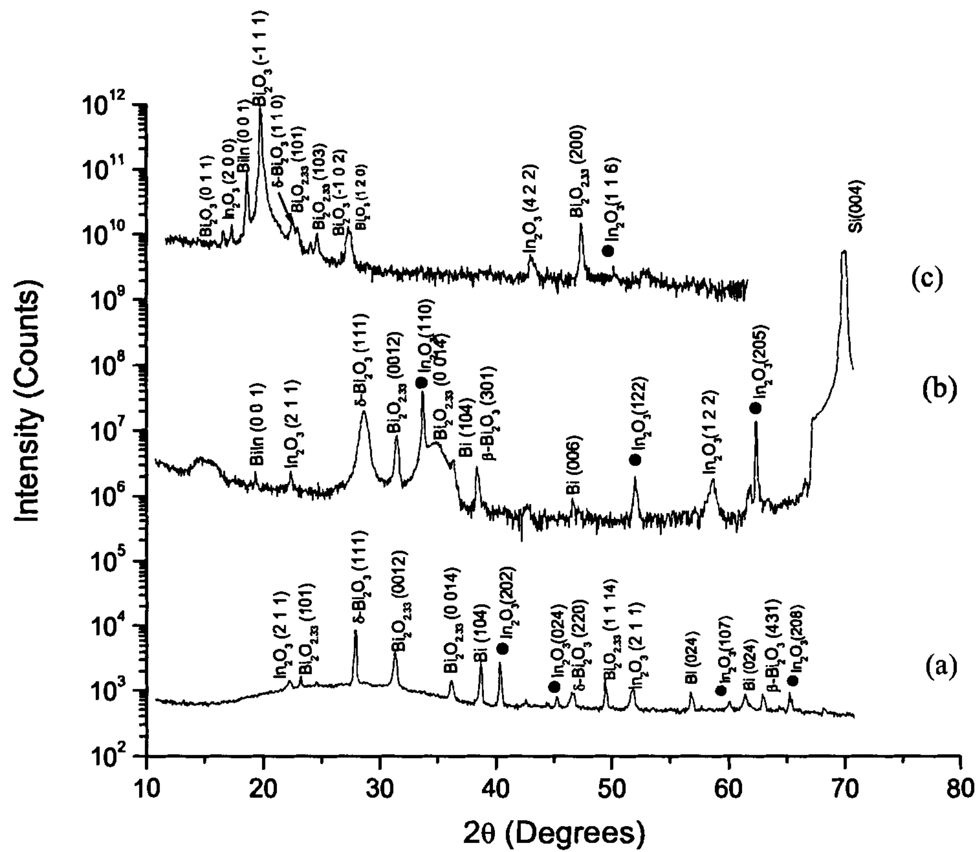


Figure 3.5: XRD scans of the same films in Fig. 3.4 after laser-annealing in air at 0.9 W laser power, (a) glass 90/90 nm, and (b) Si (100) 120/120 nm and (c) Si(111) 45/45 nm (samples D, E, F in Table 2.1). The marked (•) indium oxide is refers to the rhombohedral structure of this alloy and the unmarked one is refers to the cubic structure.

the same mixture cooled down outside the glove box, in air, we have a mixture of indium and bismuth binary oxides, as seen in spectrum (b) in Figure 3.6. The detailed results and analysis are found in Table A.8 and A.9. there are no InBiO ternary alloys listed in the data bases or found in the literatures. Therefore, we can't rule out their existence in our materials.

### 3.1.3 TEM Results

Samples of Bi/In deposited on pre-thinned Si(001) substrate did not result in electron transparent regions. The pre-thinned regions were likely destroyed during the process. Ion milling after processing was more successful, however, the first sample attempted was over milled. It is important to cool the sample during milling.

Figure 3.7 shows a plan view TEM and selected area diffraction (SAD) pattern of the 12/12 nm film (sample A in Table 2.1) on Si(001) that was thinned by ion milling. We conclude from the diffraction pattern that the film had been ion milled away from the silicon substrate during the milling process, and that the substrate was damaged forming poly - Si. It is good to know that is a trivial to make a TEM sample deposited on substrate. So that's good to study on more suitable substrate for sample preparation for TEM measurements.

Analysis of TEM SAD patterns is based on a converted form of Bragg's law (Eq. 3.1). The d-spacing is related to the spot position on a SAD pattern by the relation:

$$d = L\lambda/R, \tag{3.1}$$

where d = atomic spacing, R = distance to a spot on a negative, and $\lambda$ = 0.002507 nm, is the wavelength of 200 KeV electrons. The camera length, L, a constant for a given TEM is calibrated from a known SAD pattern. We used a GaAs SAD pattern to determine L which was found to be 10 % less than the value shown on the TEM when the images were obtained: L = 0.72 m (instead of 0.8 m)

Shown in Figures 3.7 - 3.11 are BF images and SAD patterns from 12/12 nm Bi/In film deposited directly on carbon or SiO-coated grids (sample G in Table 2.1), respectively as-deposited or furnace-annealed. SAD analysis and details are given in Table A.10. The TEM images confirm the XRD results regarding a polycrystalline structure for Bi/In films before and after annealing. They also show that the BiIn alloy during sputtering, Furnace annealed

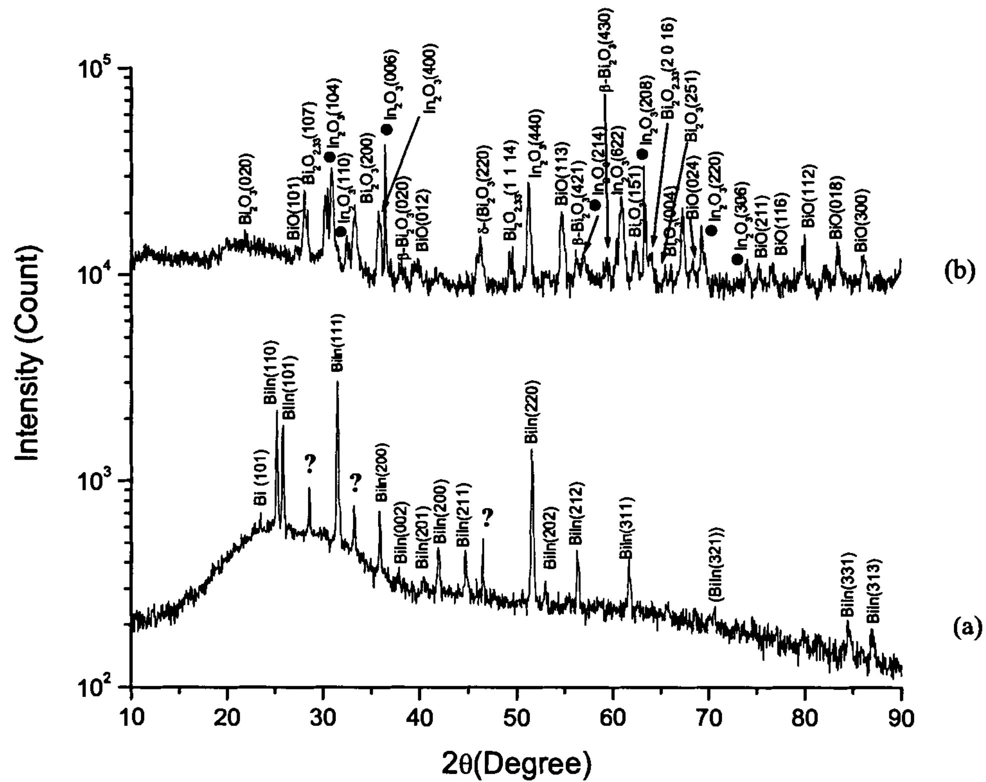


Figure 3.6: XRD data of solid In/Bi melted in $N_2$ by heating to 270°C and cooling to room temperature in (a) $N_2$ and (b) in air. The marked (•) indium oxide is refers to the rhombohedral structure of this alloy and the unmarked one is refers to the cubic structure.

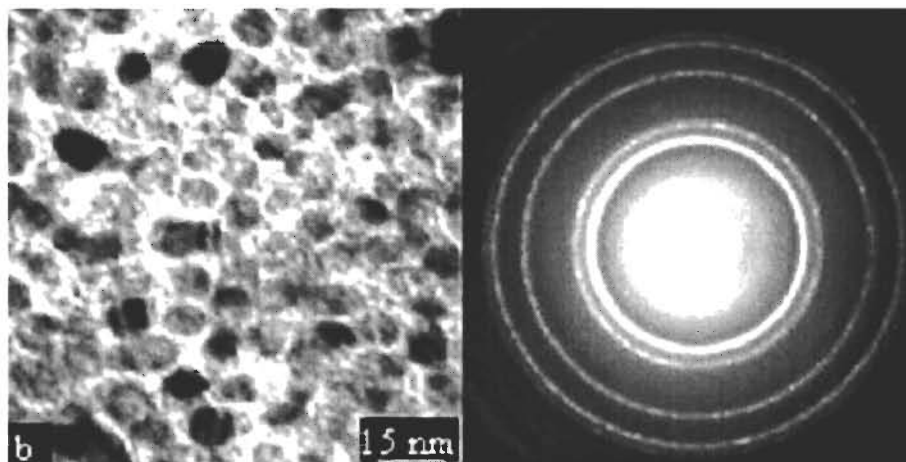


Figure 3.7: TEM planview and SAD images from an ion milled 12/12 nm Bi/In laser-annealed in air but damaged by ion milling. The SAD shows only poly - Si diffraction.

films form a mixture of bismuth and indium oxides as was observed for laser-annealed films by XRD. We attempted to laser anneal the films on TEM grids but this failed as the films shattered. Details are included in tables that are listed in appendix A (A.10- A.14).

The BF images show that the grain sizes of the Bi/In as deposited films are in the range of 50 nm to 300 nm. There are also smaller grains of size 5-10 nm in between larger grains. Grains are separated by bright grain boundaries or thinner material, and smaller grains in some of the bigger grains are observed. Regions of different shades were observed within each grain, which indicates that the grains were not all at the same orientation. By comparing the images of the as-deposited and the furnace heated films, it was concluded that the range of the grain sizes and their shapes did not change significantly after furnace heating.

Shown in Fig. 3.12 is a TEM BF image and SAD of a laser-annealed film on Si(001) obtained using mechanical polishing followed by ion milling at liquid nitrogen temperature. A BF image of samples that were heated by laser and cooled in ambient conditions showed grain sizes that did not exceed 50 nm, much smaller than those observed in the furnace annealed films. Relatively small grains are perhaps a consequence of rapid heating and cooling. Nevertheless, the same Bi and In oxides have formed. Analysis and details are given in Table A.14.

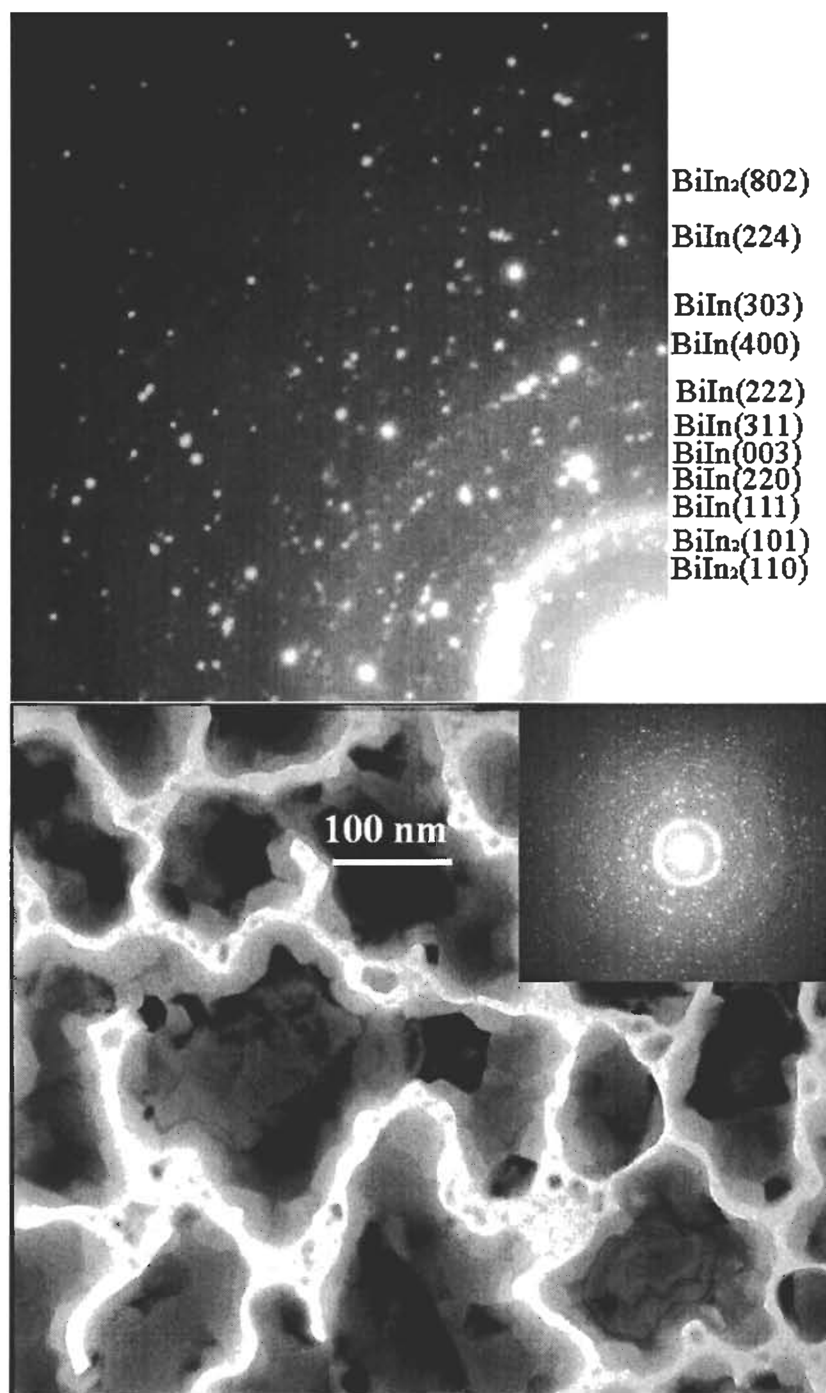


Figure 3.8: TEM BF image with corresponding SAD: 12/12 nm Bi/In as-deposited on SiO support grid.

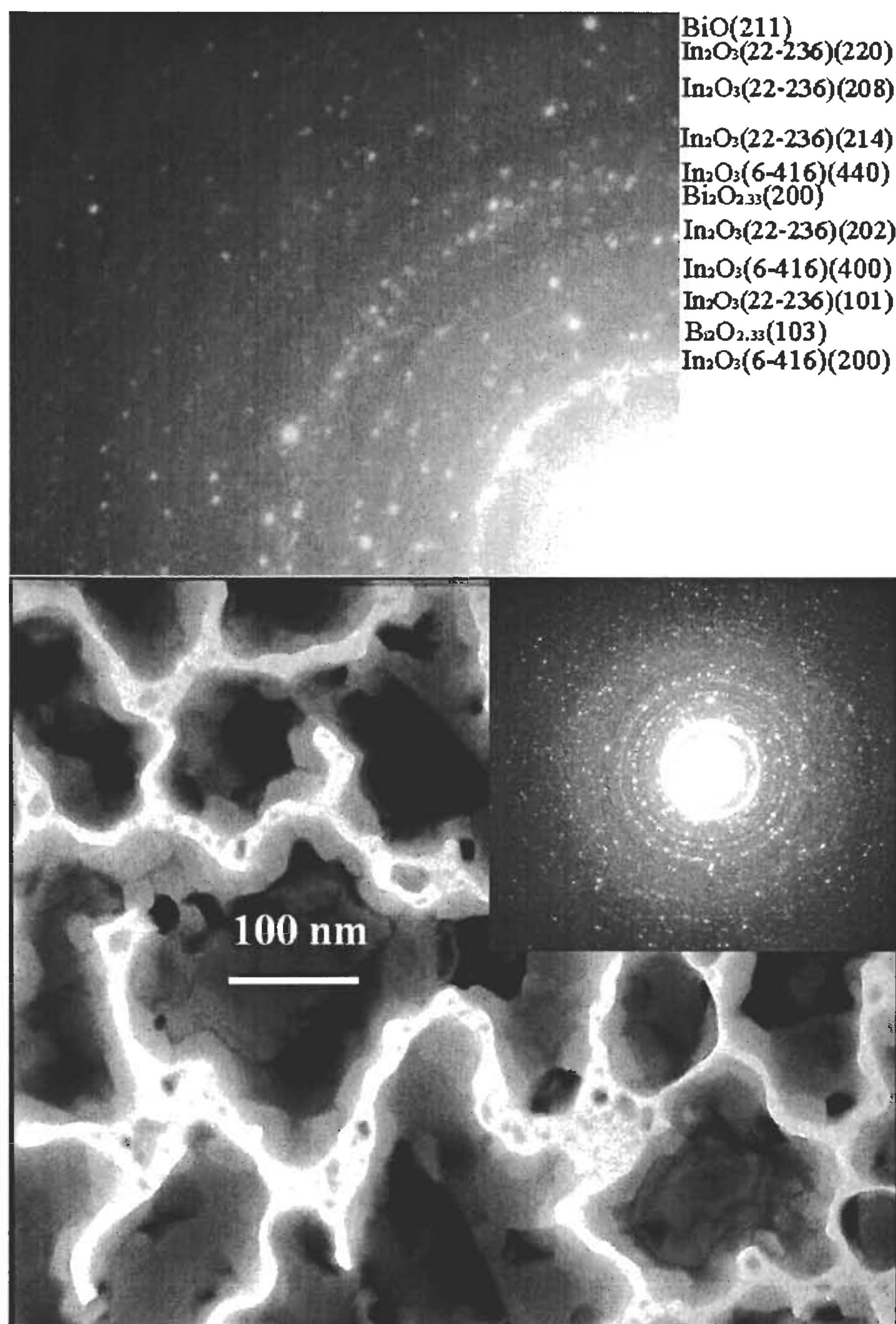


Figure 3.9: TEM BF image with corresponding SAD of 12/12 nm Bi/In on carbon support grid heated in a furnace at 150 °C.

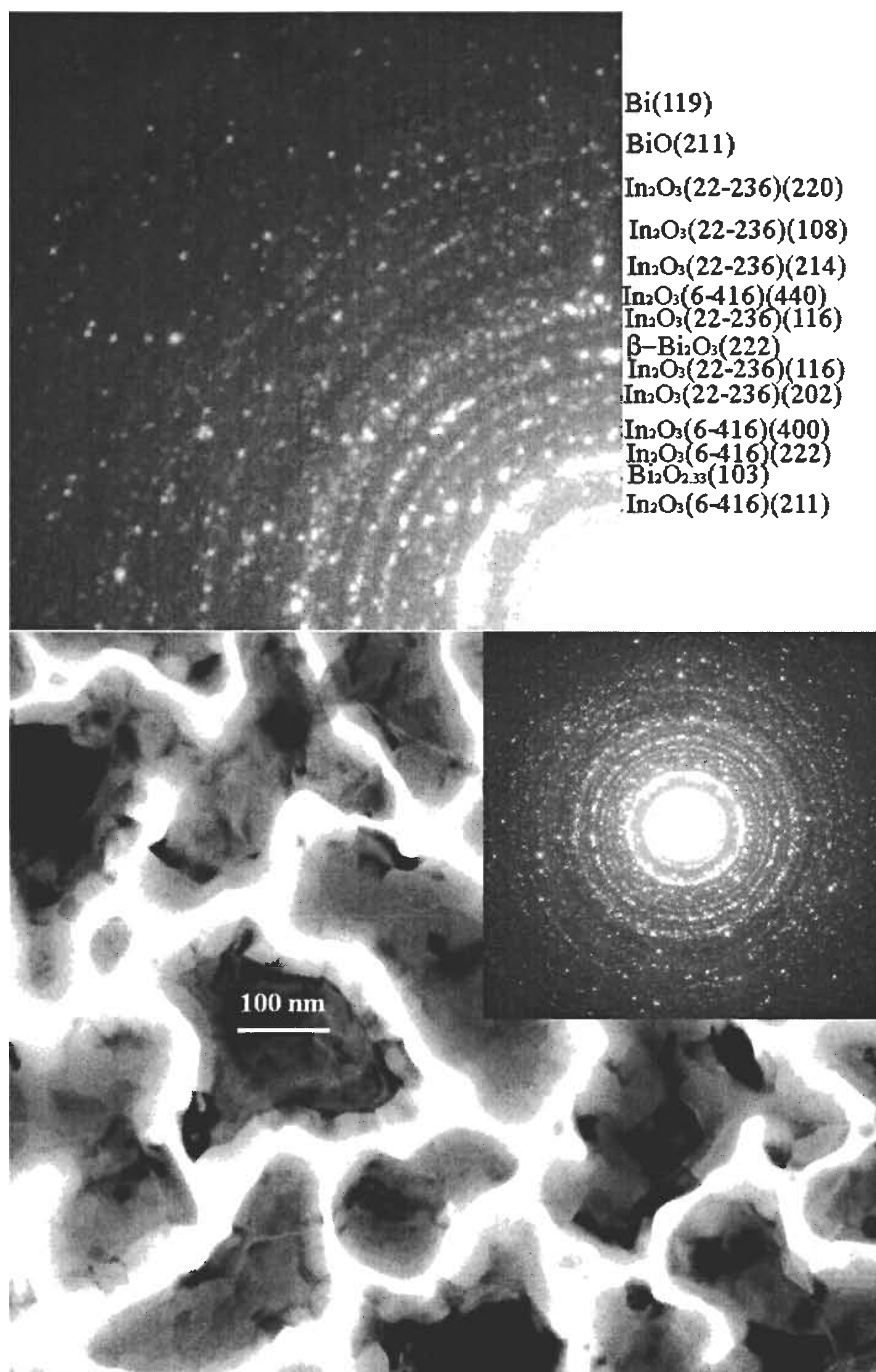


Figure 3.10: TEM BF image with corresponding SAD of 12/12 nm Bi/In on carbon support grid heated in furnace at 200 °C.

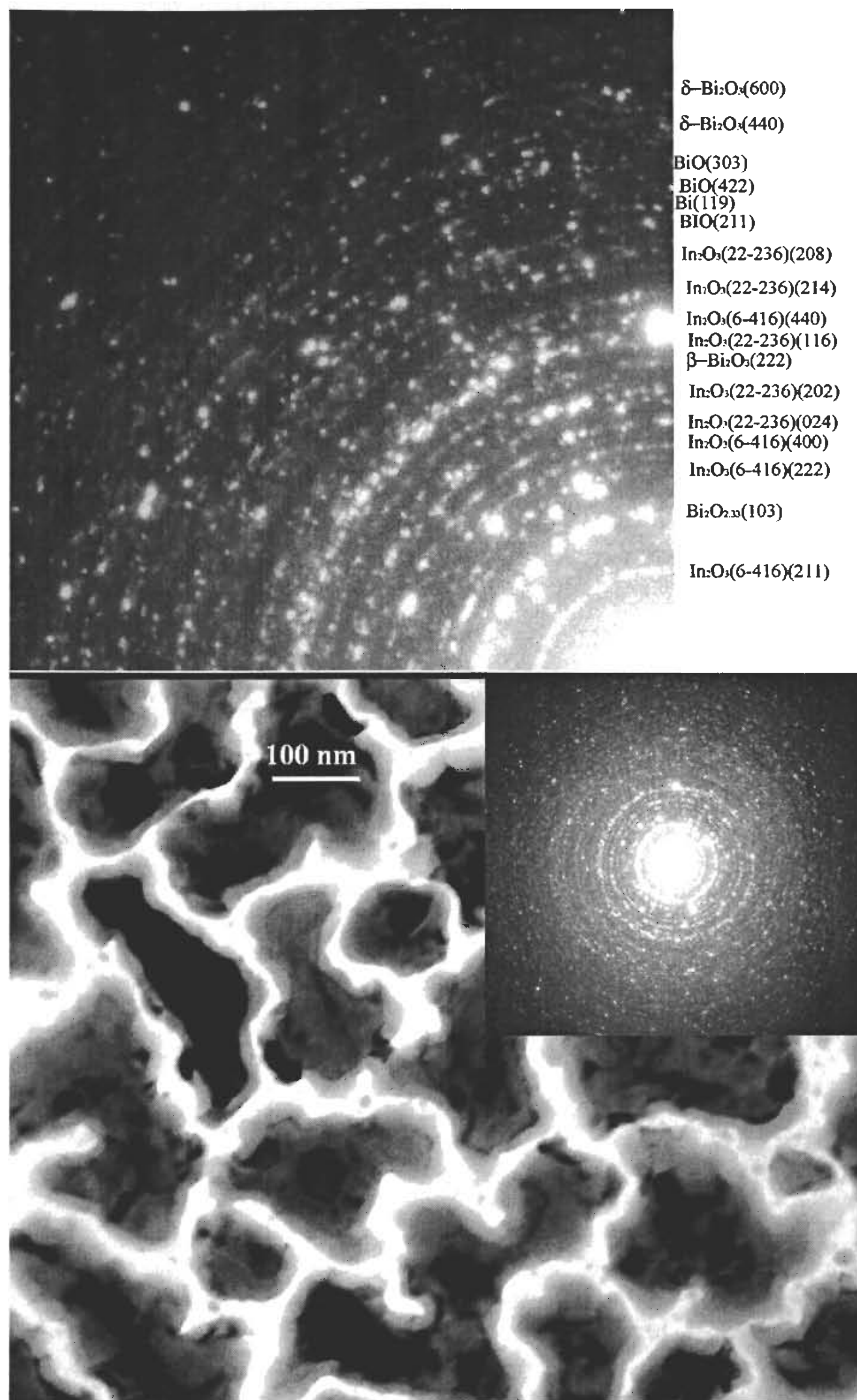


Figure 3.11: TEM BF image with corresponding SAD of BiIn, on SiO support grid furnace-annealed at 246 °C.

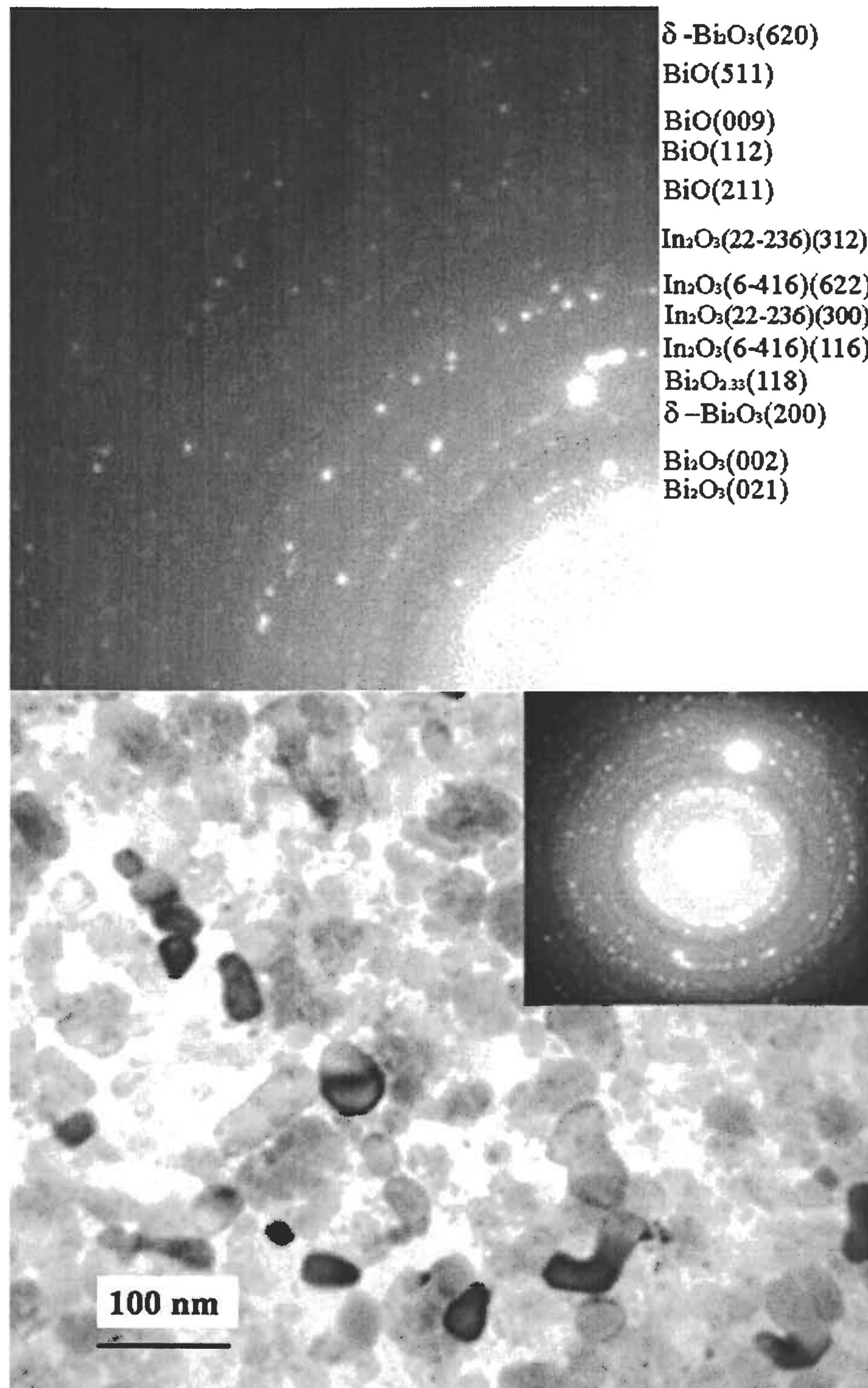


Figure 3.12: TEM planview image and SAD from an ion milled 12/12 nm Bi/In film on Si(001) laser-annealed in air.

STEM HAADF analysis of the same TEM sample in Fig. 3.12, in combination with energy dispersive X-ray spectroscopy is shown in Fig. 3.13. The image in (a) shows the formation of grains of average size 50 nm. The brighter regions in the HAADF image have higher density or thickness. Line scans of EDS shows that the In concentration is higher in the brighter regions, while the concentration of Bi atoms is almost constant.

The films are polycrystalline in both as-deposited and after annealing by laser or furnace consistent with XRD results. In-plane orientation of the film is totally random. The oxidization phases found are: $In_2O_3$ with different structures (cubic and rhombohedral), $Bi_2O_3$, $\beta$- $Bi_2O_3$, $\delta$- $Bi_2O_3$, $Bi_2O_{2.33}$ and BiO. The island size, which was measured manually, is larger after furnace heating compared to laser, 100 nm versus 50 nm. A non-uniform distribution of In is detected after laser-annealing as shown by HAADF. The In composition is greatest in the brighter regions (thickness and/or composition effects).

## 3.2 Surface Morphology

### 3.2.1 SEM Results

SEM images of Bi/In 12/12 nm films deposited on grids and heated in a furnace at 150°C, 200, and 246°C (Sample G in Table 2.1) are shown in Figure 3.14 (a), (b), and (c). From these images it is clear that the island diameter ranges between 50 nm to 800 nm and did not change after heating. The island sizes are larger than those obtained from TEM of 12/12 nm films, 100 - 200 nm but this may be the result of different substrate types, grids versus Si(001).

We can see from the SEM images of Figures 3.15 - 3.17 for Bi/In (45/45 nm) on various substrates, that the laser annealing process results in holes but the as-deposited island formation is still visible on the surface after annealing. The laser-annealed samples show holes on the surface of the film likely because of melting, gas emission, or expansion. The most severe hole formation can be seen in the images of laser-annealed sample on the $SiO_2$/Si(001) substrate shown in Figure 3.17.

The other noticeable point about our laser annealed samples is that films on silicon substrates have a significantly broader width between the as-deposited and laser annealed segments that it is not visible for samples with a glass substrate. Figure 3.18 and 3.19

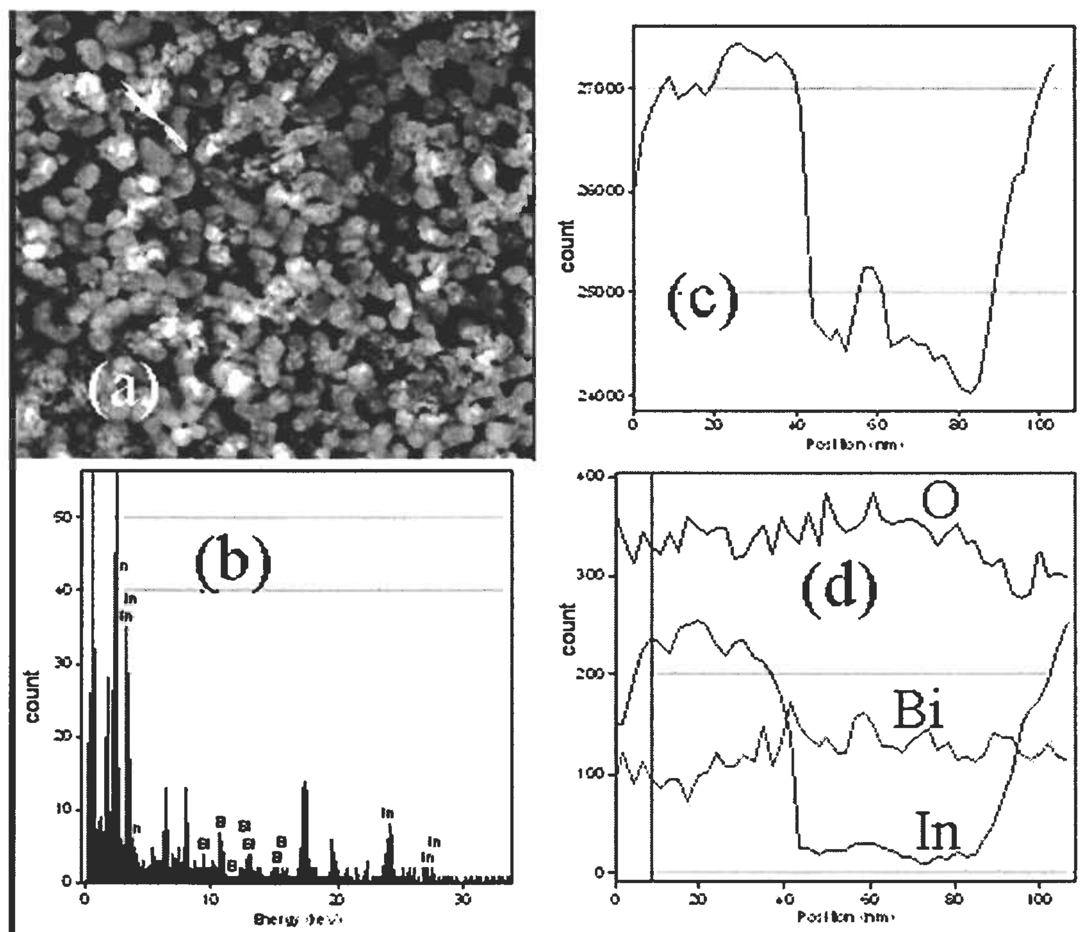


Figure 3.13: (a) High angle annular dark field (HAADF) image, (b) EDS spectra from one spot, (c) HAADF intensity along indicated line in image, (d) results of EDS along the line for Bi, In, and O. .

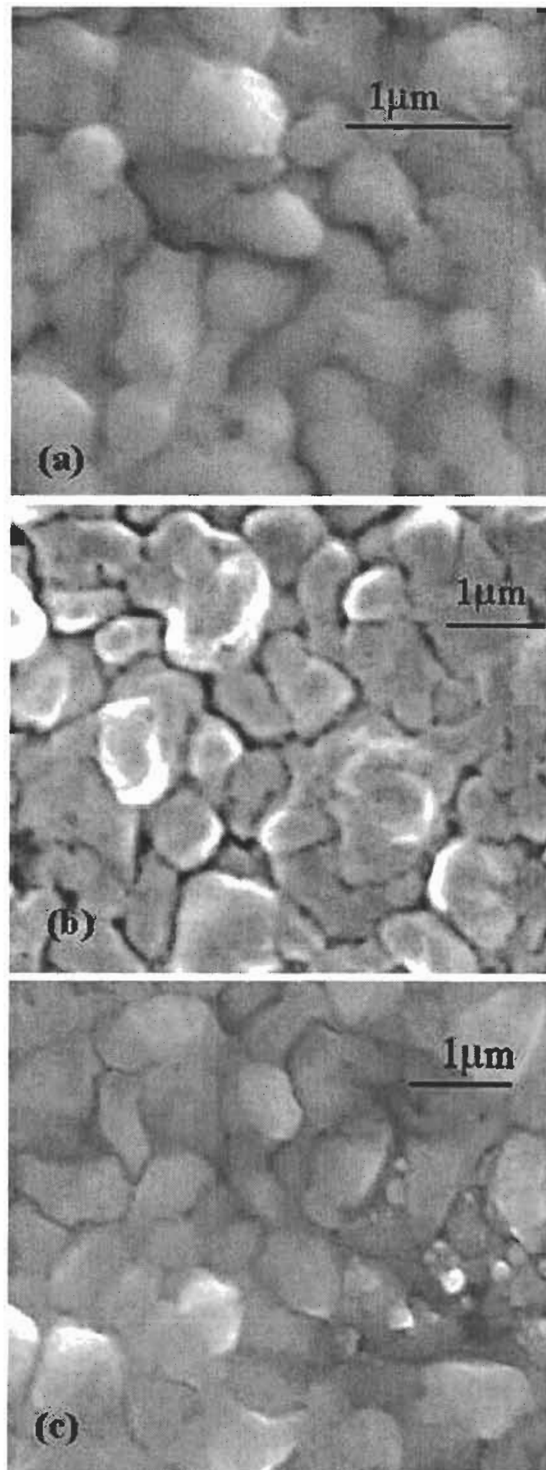


Figure 3.14: SEM image of BiIn (12/12 nm) on Si(001) (a) as-deposited and heated at (b) 150°C and (c) 200°C (e-beam voltage 5kV).

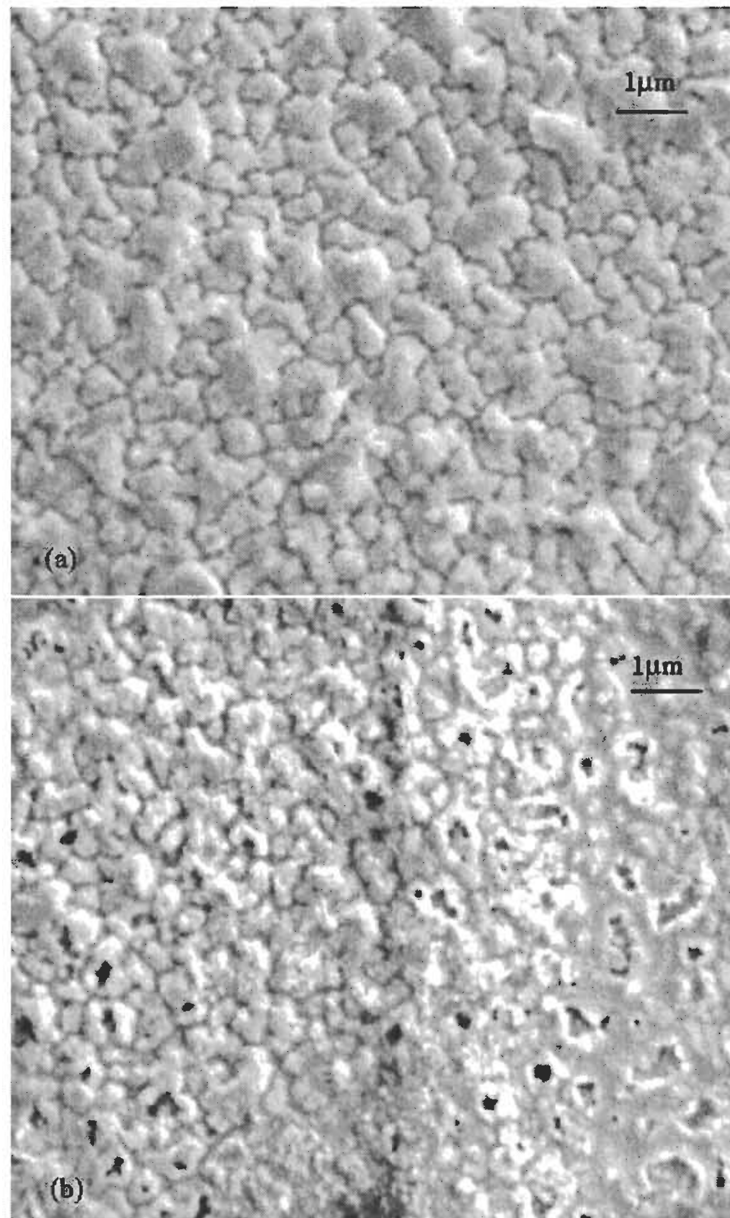


Figure 3.15: SEM image of a Bi/In (45/45 nm) on Si(001) (a) as-deposited and (b) laser-annealed (e-beam voltage 15 kV).

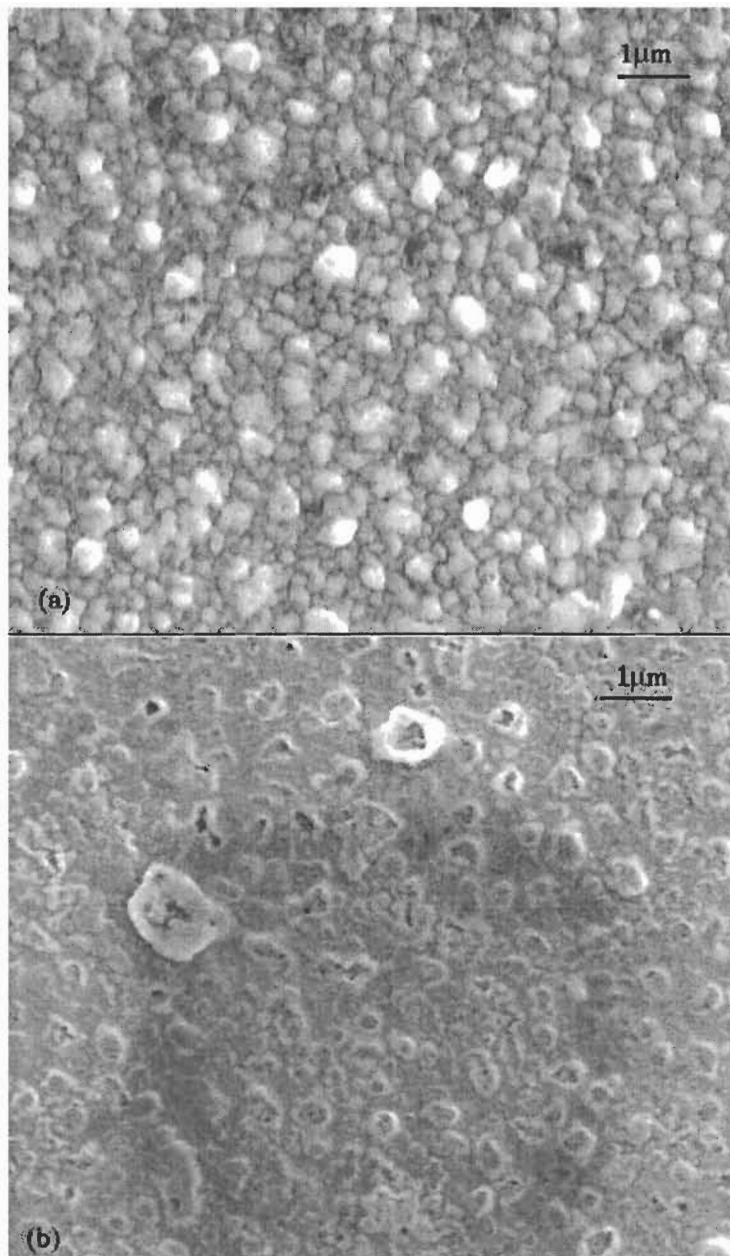


Figure 3.16: SEM image of BiIn (45/45 nm) on $Si_3N_4$/Si(001) (a) as-deposited and (b) laser-annealed (e-beam voltage 12 kV).

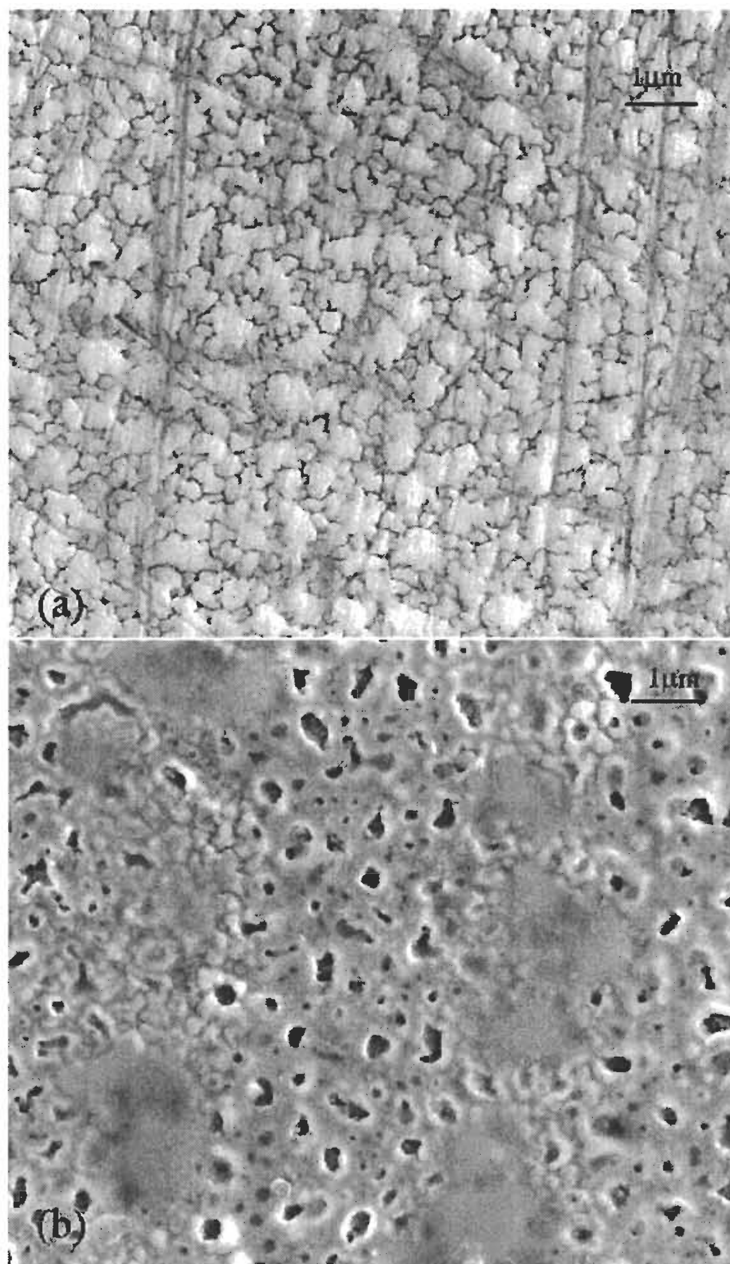


Figure 3.17: SEM image of BiIn (45/45 nm) on $SiO_2$/Si(001) (a) as-deposited and (b) laser-annealed (e-beam voltage 15 kV).

show SEM images at the border between annealed and unannealed regions for glass and Si(001) substrates. The heat conductivity of glass is much less than for silicon substrates. Therefore, less lateral heat conduction occurs and the film heating is more localized to the laser spot.

Laser annealing causes holes to form in the film. The average island sizes were in the range of 50 - 800 nm, comparable to the TEM result. The larger border between as-deposited and laser-annealed regions on glass substrates compared to Si substrates can be explained by the lower heat conductivity of glass in comparison with Si. There is evidence of loosed shape (non-grainy shape) film in Si substrate after double heating in scanning process on the border.

### 3.2.2 AFM Results

Non-contact AFM images of Bi/In as-deposited and laser-annealed samples with total thicknesses 90 nm (45/45 nm) on glass and Si (001) substrates (sample C in Table 2.1) are shown in Figure 3.21. No variation was observed for samples deposited on silicon substrates (Si(001), Si(111), $SiO_2$, $Si_3N_4$). Larger feature sizes are seen for the glass sample compare to Si.

In Figure 3.22 and 3.23 from line profile measurements, we can conclude that the films before and after annealing have about the same root mean square (RMS) roughness 20 - 30 nm. The roughness can be due to the fact that the thickness of the films is not uniform from sputtering on the substrate. Also surface diffusion to form islands likely occurs.

We had a look at thin samples Bi/In (12/12 nm) to investigate the affect of thickness on surface morphology. There was not a noticeable change in morphology and feature size, or roughness as a function of thickness.

A 3D non-contact image of a Bi/In film on $Si_3N_4$/Si(001) is shown in Figure 3.24. The average roughness of the as-deposited is comparable to that of the laser-annealed film. Contact AFM images are shown in Fig. 3.25 (a) planview and and (b) 3D images to compare with non-contact images. The average roughness of as-deposited films is 30 nm, 22 nm and 23 nm for laser-annealed and furnace-annealed, respectively. The average roughness does not change significantly after annealing but the surface has a smaller distribution of roughnesses.

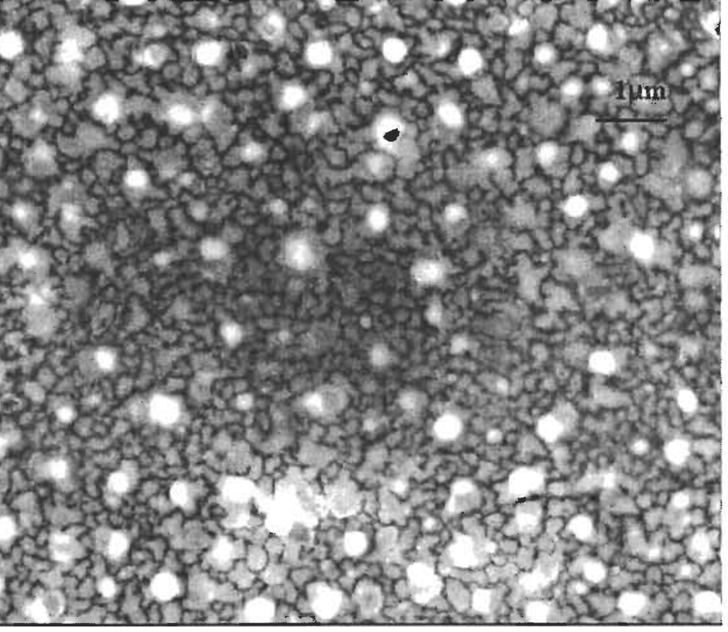


Figure 3.18: SEM image of BiIn as-deposited (45/45 nm) on glass (e-beam 15kV).

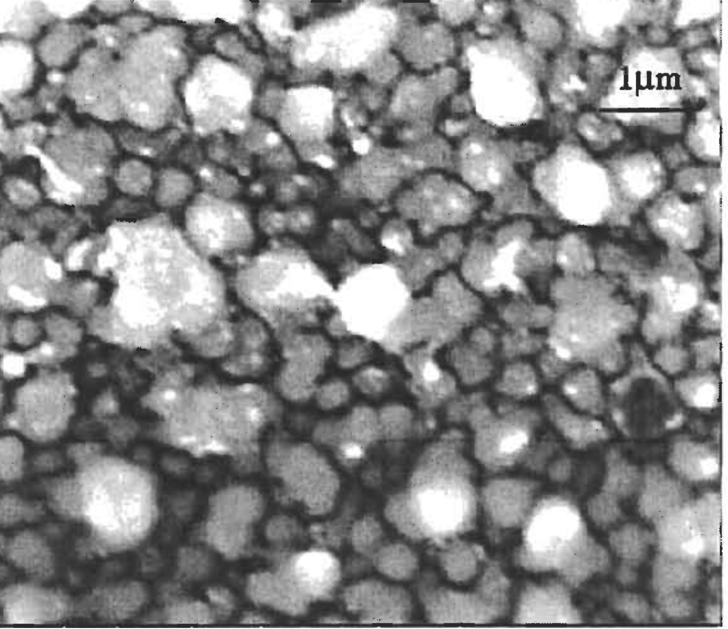


Figure 3.19: SEM image of BiIn (45/45 nm) on glass at the border of laser-annealed and as-deposited regions (e-beam voltage 15 kV).

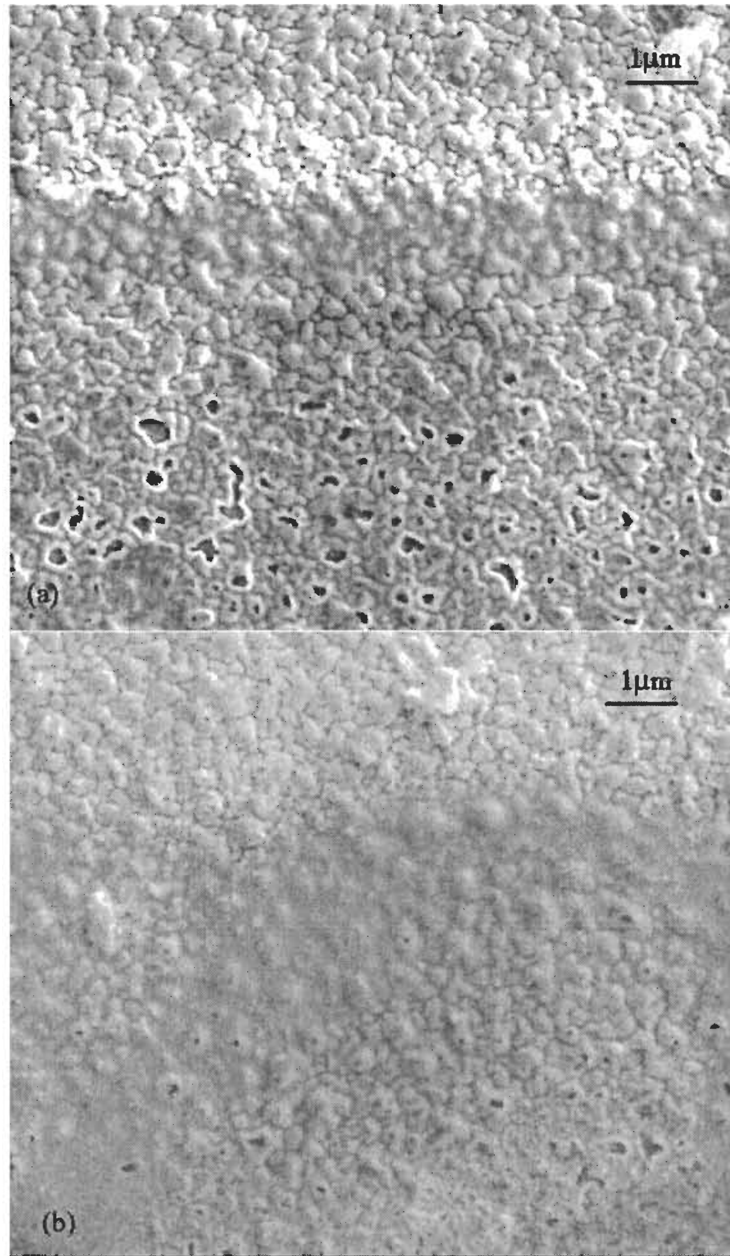


Figure 3.20: SEM image of BiIn (45/45 nm) on at the border of laser annealed and as-deposited regions (E-beam voltage 5kV) for (a) $SiO_2$/Si(001) and (b) Si(001) (e-beam voltage 5 kV).

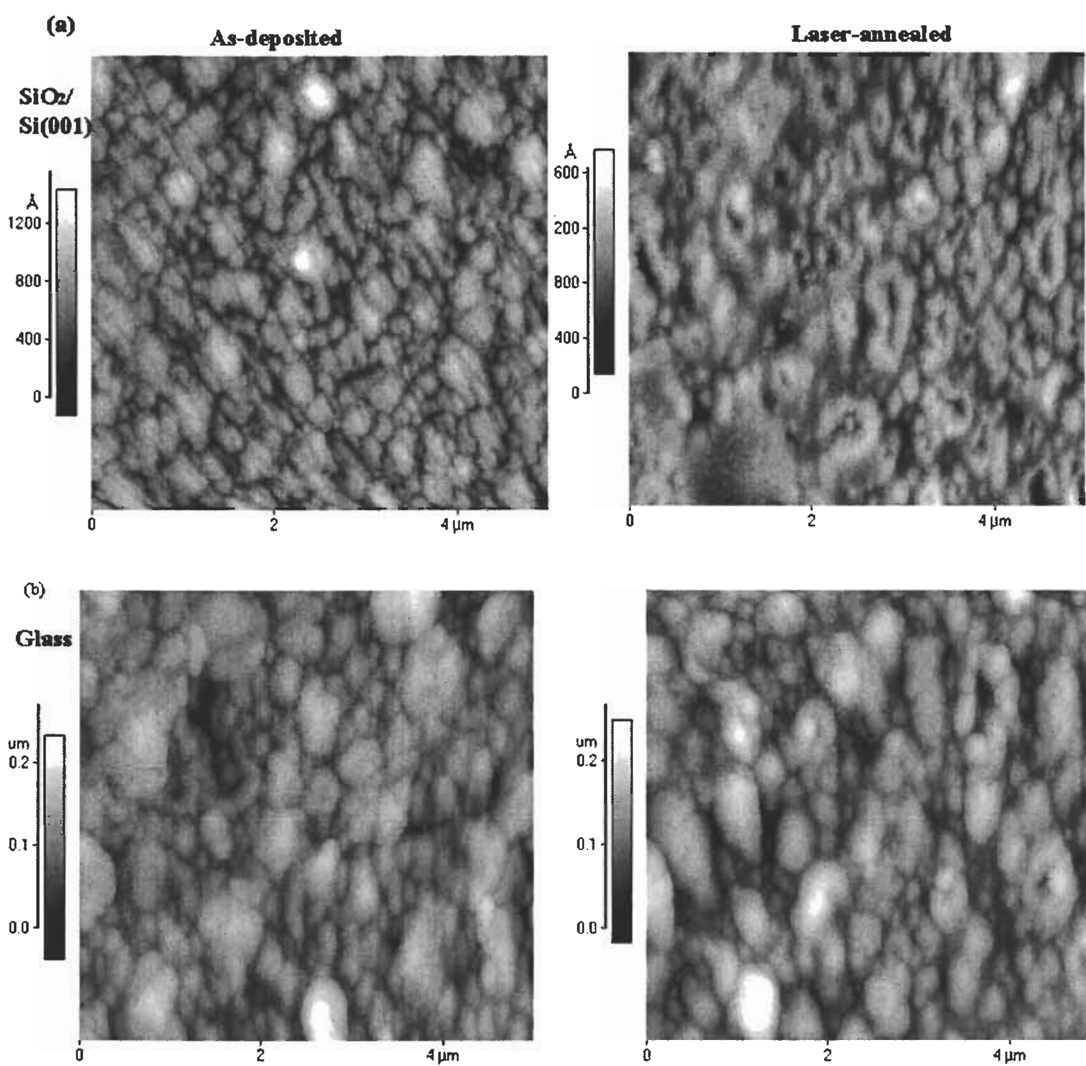


Figure 3.21: Non-contact AFM images of 90 nm (45/45 nm) Bi/In as-deposited and laser-annealed film on (a) $SiO_2$/ Si(001) and (b) glass substrate.

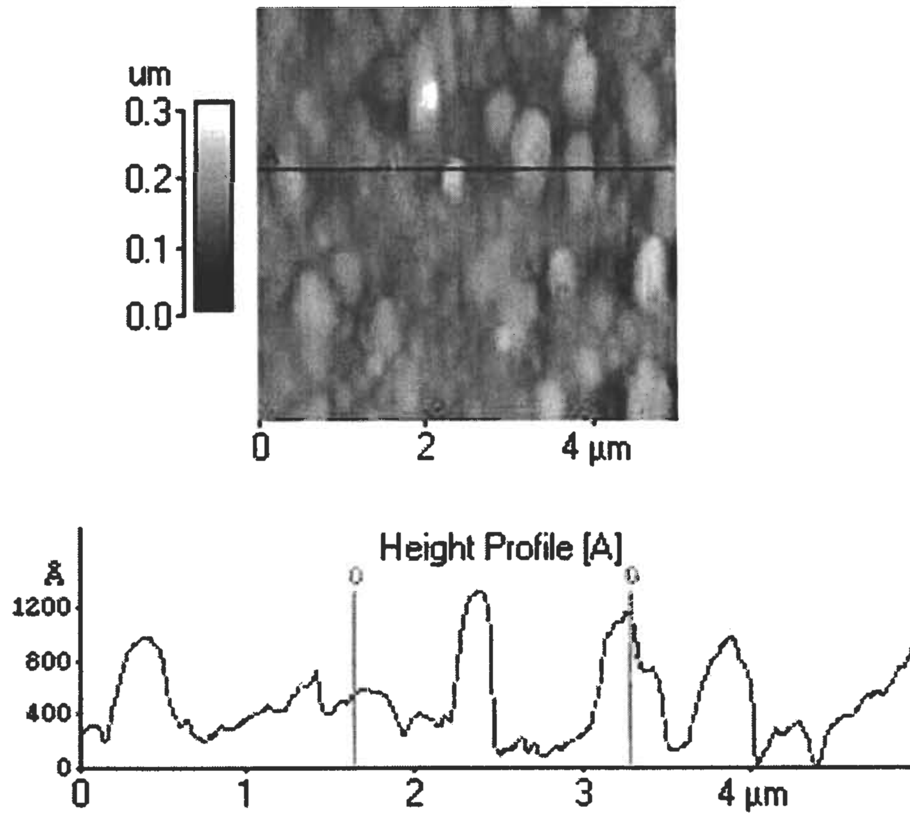


Figure 3.22: Height analysis of AFM data from as-deposited Bi/In film on top of glass, fig. 3.21 (b)

Table 3.1 lists the RMS roughness of all samples measured. These results do show that the laser annealed samples are more uniform in roughness than the as-deposited films. Furnace annealing also had no effect on the roughness measured.

## 3.3 Material Composition

### 3.3.1 RBS Results

RBS spectra from as-deposited, furnace-annealed (Figure 3.2), and laser-annealed (Figure 3.27) 120/120 nm, (sample D Table 2.1), bilayer films are shown in . The results clearly

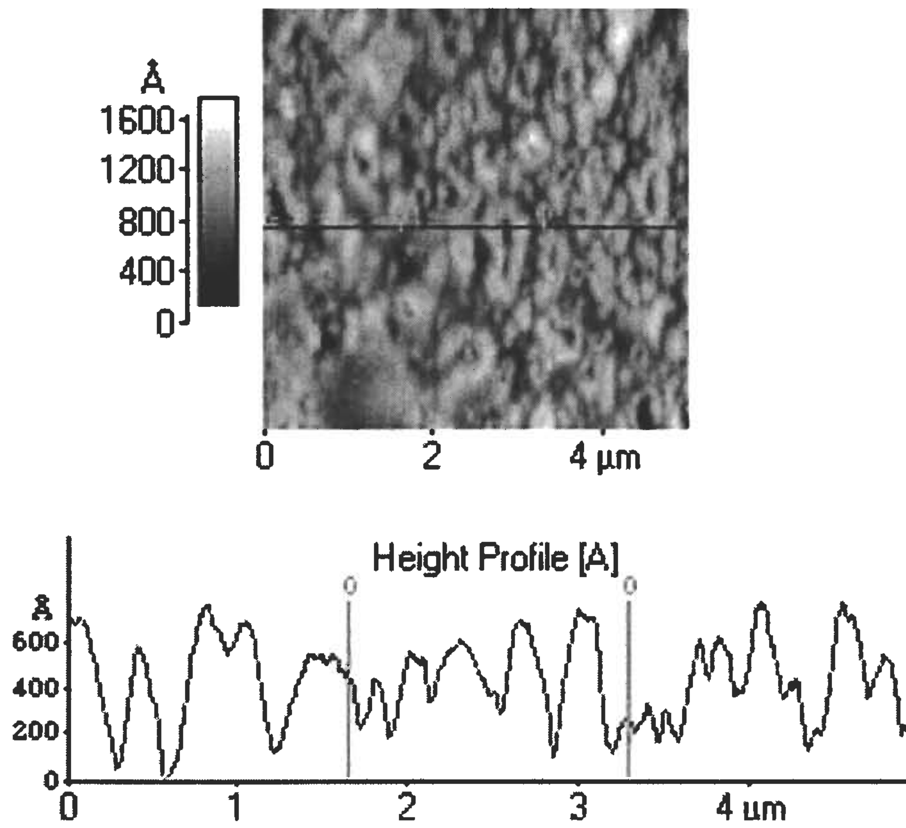


Figure 3.23: Height analysis of laser-annealed Bi/In film on a $SiO_2Si(001)$ substrate, fig. 3.21 (b)

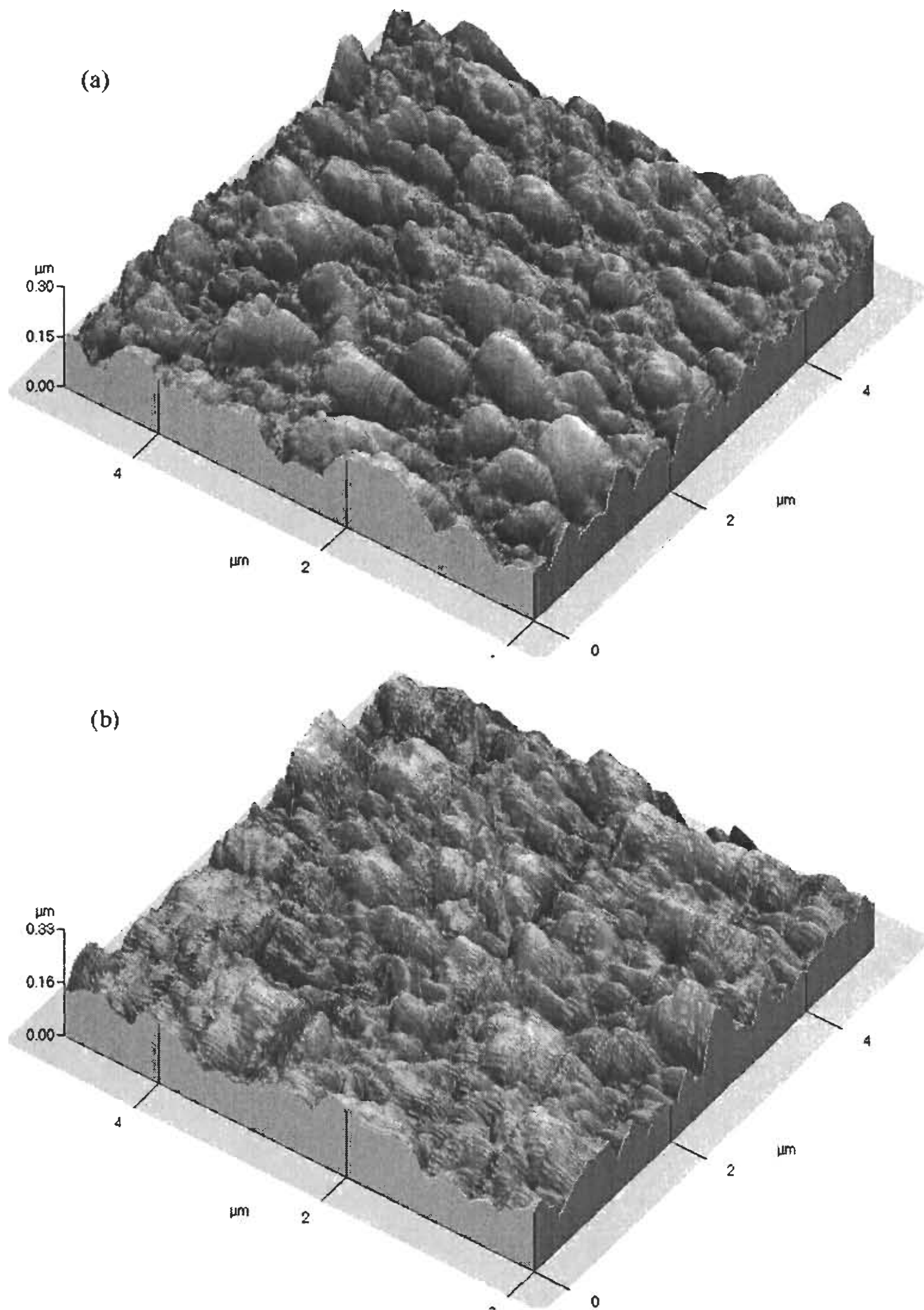


Figure 3.24: 3D non-contact AFM pictures of (a) as-deposited and (b) laser annealed Bi/In (45/45 nm) film on a $Si_3N_4$/Si(001) substrate.

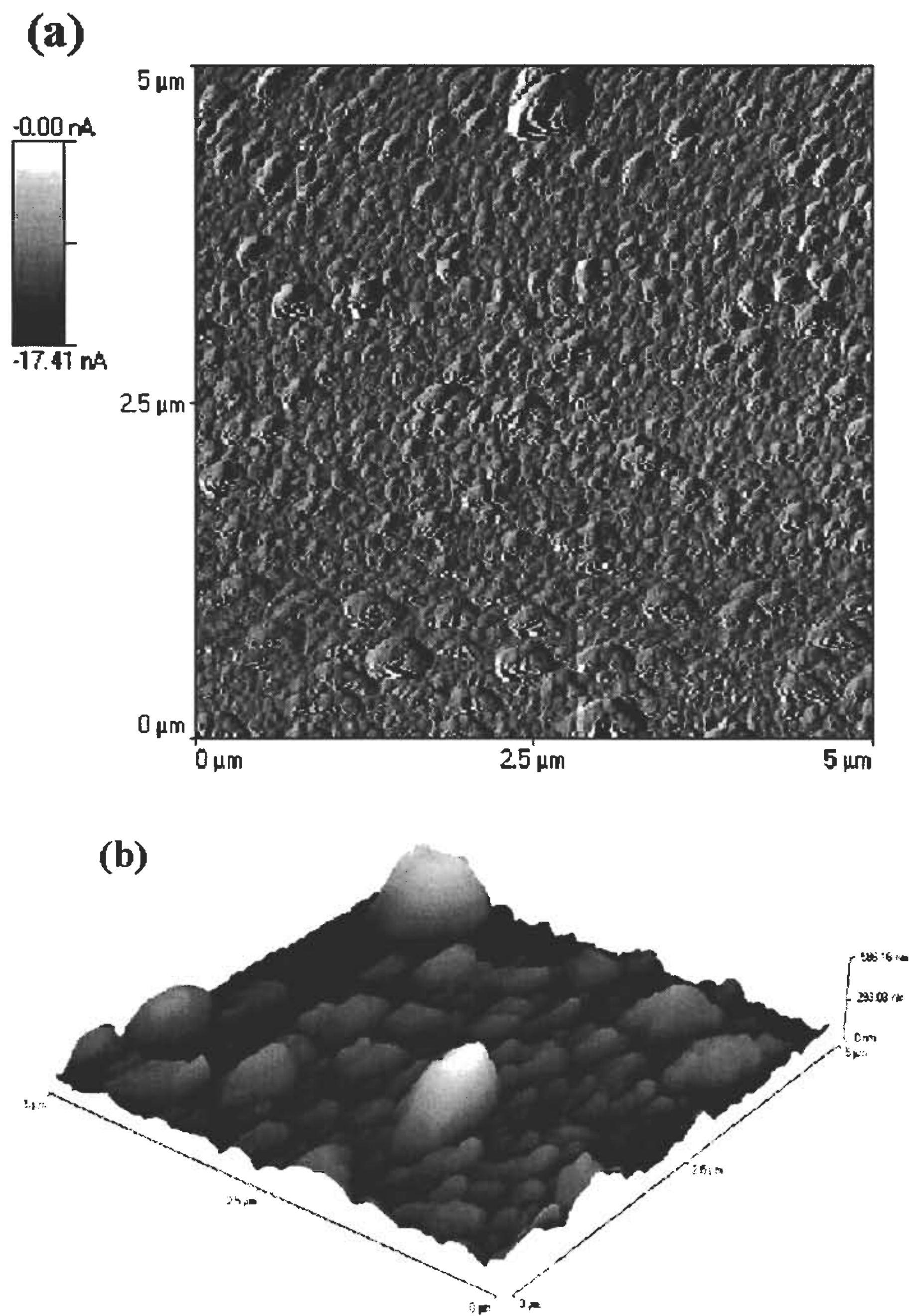


Figure 3.25: Contact AFM of 30/30 nm Bi/In as-deposited on glass: (a) AFM image (b) corresponding 3D image.

Table 3.1: AFM data for as-deposited and annealed films on silicon substrates and glass

| Sample | Substrate | Thickness | r.m.s Roughness |
|---|---|---|---|
| | | nm±1 | nm |
| as-deposited | Glass | 45/45 | 27 |
| | $Si_3N_4$/Si(001) | | 32 |
| | $SiO_2$Si(001) | | 40 |
| | Si(001) | | 19 |
| laser-annealed | Glass | | 21 |
| | $Si_3N_4$/Si(001) | | 23 |
| | $SiO_2$Si(001) | | 23 |
| | Si(001) | | 20 |
| As-deposited | Glass | 12/12 | 22 |
| Furnace-annealed | Glass | 12/12 | 28 |
| | Si(001) | | 19 |

show that for as-deposited film In is detected on the surface even though it is deposited first, next to the substrate. Simulation showed that the as-deposited film had a 2.5 nm $In_2O_3$ surface layer and a 200 nm thick $Bi_1In_{1.4}O_{0.06}$ film beneath it. After laser annealing, oxidation of the complete film was easily detected while furnace-annealing only caused surface oxidation of the films. Table 2.2 summarizes the oxygen content obtained from the NRA and RBS data. RBS indicates that the surface thin layer (2.5 nm) of Indium Oxide acted as a protective shell during furnace-annealing preventing the rest of the film from reacting with oxygen compared to laser annealing ($BiIn_{0.6}O_6$ /$Bi_{0.3}InO_6$ bilayer of average thickness 200 - 245 nm below it). The laser anneal heating process is fast and alloys the oxygen likely from adsorbed water before it can evaporate. In furnace annealing, water has the opportunity to evaporate and escape from the surface of the film before oxidation.

In total we can conclude that Bi/In thin film is: a transparent - conductive Indium Bismuth Oxide (IBO), with meta-stable phases, a large percentage amount of oxygen, that varies depending on the heating method (furnace or laser).

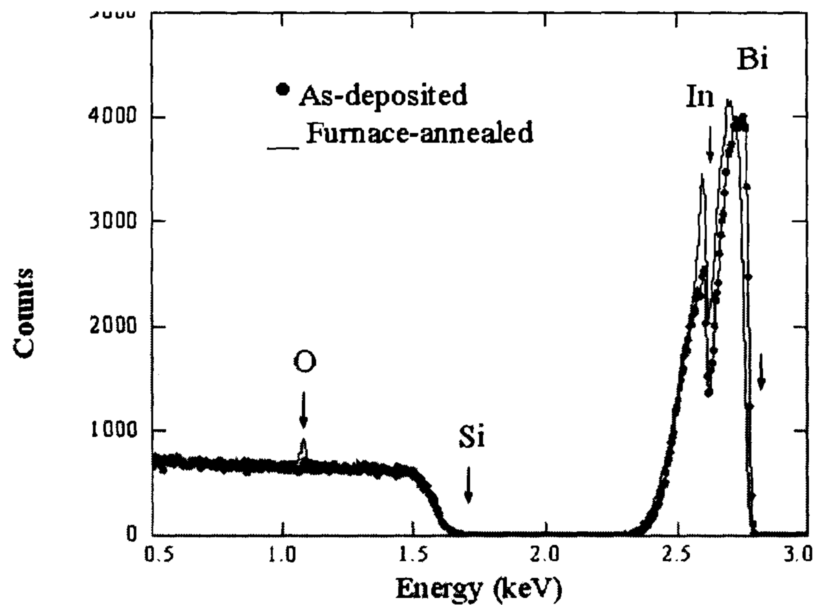


Figure 3.26: RBS spectra of Bi/In/Si(001) 120/120 nm thick samples, as-deposited (circles) and furnace annealed at 250°C (line). The arrows indicate the energy position of the element if it were at the surface. The shift in the Bi peak to lower energies with respect to the surface energy position, with the In peak being at the surface position indicates the presence of a thin (20 nm) surface In oxide layer in the as-deposited film. The degree of surface In oxidation increases after furnace annealing as seen by the surface oxygen peak and the increased shift in the Bi peak with no change in the In.

Table 3.2: RBS/NRA results of oxygen concentration in 120/120 nm Bi/In/Si samples.

| Sample | [O] NRA ($10^{17}$ at./cm$^2$) | O% | [O] RBS ($10^{17}$ at./cm$^2$) | O% |
|---|---|---|---|---|
| As-deposited | 0.22 | 0.4 | 0.27 | 0.5 |
| 150°C furnace-annealed | 0.87 | 1.58 | 0.84 | 1.52 |
| 200°C furnace-annealed | 0.80 | 1.45 | 0.70 | 1.27 |
| 246°C furnace-annealed | 1.5 | 2.72 | 1.3 | 2.3 |
| Laser-annealed | 9.5 | 17.23 | 13.5 | 24.50 |

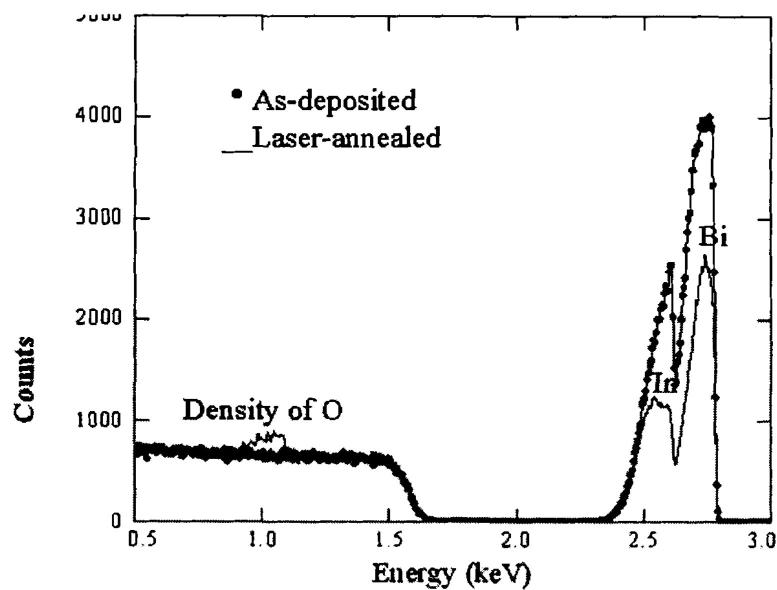


Figure 3.27: RBS spectra from Bi/In/Si(001) 120/120 nm thick samples as-deposited (circles) and laser annealed (line), showing a large increase in oxygen content throughout the film and a reduction in the density.

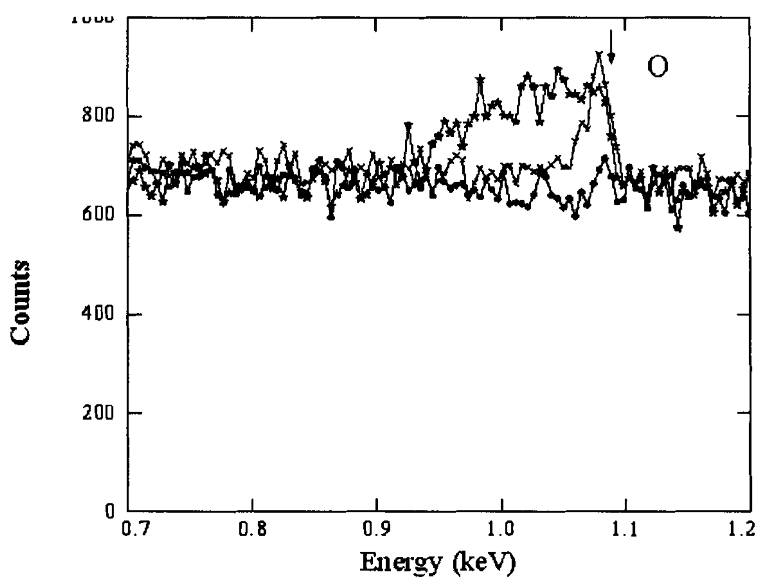


Figure 3.28: RBS spectra showing the oxygen peak from Bi/In/Si(001) 120/120 nm thick samples as-deposited (circles), laser annealed (stars), and furnace annealed at 250°C (crosses). This shows that the oxidation in the laser annealed samples occurred throughout the film while that of the furnace annealed occurred only at the surface.

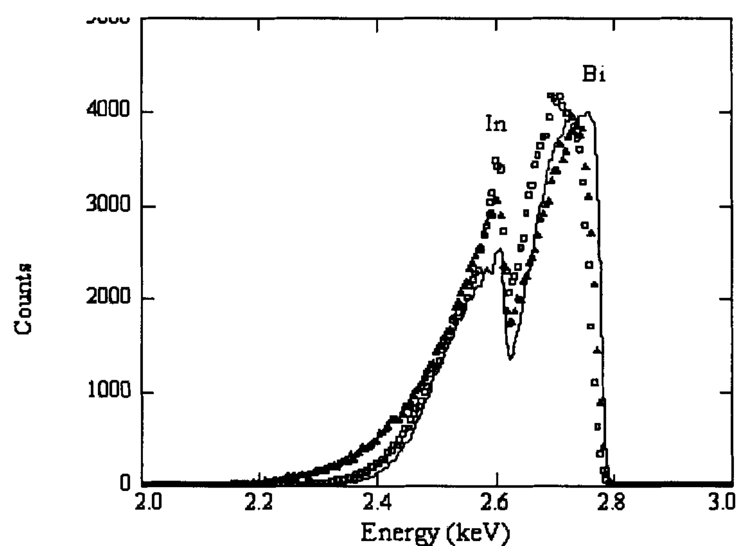


Figure 3.29: RBS spectra showing the Bi and In peaks from Bi/In/Si(001) 120/120 nm thick samples as-deposited (solid line), furnace annealed at 150°C (solid triangles) and 250°C (open squares). The lower energy tail is greatest for the 150°C furnace anneal indicating the film roughened further compared to the as-deposited and 250°C anneal. The shift in the Bi peak is greatest for the 250°C anneal which saw the greatest amount of surface oxidation.

Table 3.3: Hall measurement comparison of ITO and Laser annealed BiIn

| Sample | Substrate | Thickness | $\mu$ | n | R | ρ |
|---|---|---|---|---|---|---|
| | | nm | $cm^2/Vs$ | $\times 10^{20}$ $cm^{-3}$ | $\Omega$ $cm^{-2}$ | ($\Omega$cm) |
| LA BiIn | Si(001) | 120 | 13.56 | 2.17 | 1.84 | 22.08 |
| | $SiO_2$/Si(001) | 90 | 20.97 | 3.87 | 1.84 | 16.56 |
| | $Si_3N_4$/Si(001) | 90 | 8.25 | 0.31 | 2.28 | 20.52 |
| ITO | Si(001) | 120 | 2.85 | 6.69 | 1.89 | 22.68 |

## 3.4 Electrical Properties

We measured the electrical parameters of 45/45 nm Bi/In laser annealed samples by using the Hall effect with the Van der Pauw method (sample C in Table 2.1). One purpose of these measurements was to compare our InBi oxide films with data for Indium Tin Oxide (ITO) films in the literature [31]. For optimal conductivity, ITO films are 5-10 wt% $SnO_2$, typically 300 nm thick with a carrier concentration $\sim 10^{21}$ $cm^{-3}$ [33]. ITO on glass substrates has a surface sheet resistance $\sim$ 23.5 $V/cm^2$. The substrate temperature and oxygen pressure affect the conductivity of the ITO films.

The results of Hall measurements and 4-point probe measurements on laser annealed Bi/In are summarized in Tables 3.3 and 3.4. The Hall mobility was 8.25 $cm^2/Vs$ to 20.97 $cm^2/Vs$ for laser annealed BiIn film deposited on Si(001), $SiO_2$, or $Si_3N_4$, and 2.85 $cm^2/Vs$ for ITO deposited on Si(001). The carrier concentration on the same samples showed a range of $2.17\times10^{20}$ - $3.87\times10^{20}cm^{-3}$. Further, the sheet resistance was 1.84 - 2.28 $cm^{-2}$. The Hall effect measurement showed that there is no difference in electrical properties for Bi/In thin films on silicon substrates with or without $SiO_2$ and $Si_3N_4$ coatings. This was good evidence that there was insignificant reaction between the Bi/In and the Si substrates. The four point results show that the laser annealed sheet resistance is comparable before and after laser annealing. results for as-deposited Bi, In, BiIn and laser-annealed BiIn are listed in Table 3.4. The results show that the laser annealed is comparable to ITO[25]. So we can conclude that In/Bi/O thin film is a conductive and transparent oxide after annealing like ITO.

Table 3.4: Four-point probe sheet resistance and resistivity measurements [25]

| Sample | Thickness | Sheet Resistivity | Film Resistivity | Bulk Resistivity |
|---|---|---|---|---|
| | nm | (Ω/sq) | (Ωcm) $\times 10^{-4}$ | (Ωcm) |
| Bi | 45 | $79.6 \pm 5$ | 3.58 | $1.3 \times 10^{-4}$ |
| In | 45 | $3.5 \pm 0.2$ | 0.16 | $8.0 \times 10^{-6}$ |
| Bi/In as-deposited | 30/30 | $82.8 \pm 6$ | 4.97 | - |
| LA Bi/In | 30/30 | $80.8 \pm 5$ | 4.85 | - |

# Chapter 4

# Summary

## 4.1 Summary of structural properties

In this chapter we discuss the results and compare them to Indium Tin Oxide (ITO) already a well-known transparent conducting oxide.

We have studied the properties of Bi/In either in thin film form, deposited on various substrates as a function of film thickness and annealing conditions, or as bulk metals alloyed in $N_2$ or in air. XRD and TEM experiments indicated polycrystalline alloys (BiIn, $BiIn_2$, $Bi_3In_5$, $Bi_{0.06}In_{0.94}$ ) for as-deposited thin film samples. The Bi and In alloyed during sputtering at room temperature. The bulk metal alloying resulted in a more equilibrium mixture with one alloy BiIn present. The as-deposited thin films, however, showed often 3 phases present indicating local compositional variations.

Bi/In films deposited at room temperature show a rough island-like surface for all films. The average island size that we measured is about 10-50 nm for the as-deposited films with a 90 nm total thickness. A wide range of 50 nm to 800 nm was obtained for 120/120 nm Bi/In films on silicon, which were heated in furnace at 150°C, 200°C, and 246°C as measured by SEM.

Annealing by furnace or laser resulted in the oxidation of films to a mixture of In and Bi binary oxides. In the furnace, oxidation was feasible only for a limited thickness. The thinnest samples (12/12 nm) completely oxidized (TEM and XRD), while the thicker ones (120/120 nm) oxidized only in a surface layer (RBS). The TEM results of furnace annealing in air up to 246°C for 5 hours show the development of identifiable oxides. Plan view TEM

results from a similar bilayer deposited onto a SiO-coated copper grids that was furnace-annealed in air shows a variety of grains sizes. The film is still polycrystalline and the grain size is larger than as-deposited. XRD scans shown in related Figures in chapter 3 showed similar results to the TEM. The starting films display strong diffraction peaks consistent with BiIn alloy formation. After laser annealing the films are less diffractive and new reflections develop that begin to match some of the known BiIn oxide structures in powder diffraction databases. AFM measurements of as-deposited and laser-scanned Bi/In films (12 nm /12 nm) showed rough films (Average 21 nm RMS) with feature sizes of 120 nm. The affect of the substrate was to alter the heating and cooling rates during laser annealing. Different distributions of In and Bi oxides were observed on glass versus silicon substrates.

RBS spectra and analysis of the data from the as-deposited and laser annealed sample showed that In oxides were present on the surface of both. Since the Bi film was deposited after the In film, it is further evidence that mixing of the In and Bi films occurred during sputter deposition or at room temperature from diffusion. This result is consistent with the severe roughness observed with the profilometer, AFM results of the In and Bi films, and XRD that showed BiIn binary alloys.

The bulk alloys formed by heating Bi and In in $N_2$ formed the expected binary phases and oxidized to the same intensity of In and Bi oxides.

## 4.2 Comparison of IBO to Indium Tin Oxide

Transparent conductive oxides (TCO) have been known and employed technologically for about 100 years (1907) [26], primarily in the form of doped, single-cation oxides such as $In_2O_3$ and $SnO_2$. Beginning in 1990s, multi-cation oxide TCO were developed in Japan and the US [28].

TCOs are wide band-gap materials (Eg$\geq$ 3.70 eV) whose characteristics whether metallic, semiconducting, or insulating depend on the stoichiometry. The properties of TCO films strongly depend on the deposition technique, the deposition parameters, and their operating environment. In general: (1) TCO films are far less crystalline and ordered than the corresponding bulk materials, and (2) most attempts to induce greater crystallinity are usually accompanied by loss of conductivity.

$InO_X$ is a wide band-gap material ($E_g$~3.7 eV). $InO_X$ electrical, optical and structural

characteristics are well studied. Due to oxygen vacancies $In_2O_3$ is n-type, however, it behaves as an insulator in its stoichiometric form.

Tin-doped Indium Oxide (ITO) is an n-type wide band gap semiconductor, with an optical band gap 3.89 - 4.21 eV [33]. It is widely used in flat panel displays and solar cells due to its property of being both electrically conductive and optically transparent in the visible region. There are also other applications in the biomedical industry [30].

ITO films typically have low resistivity, $\rho$, due to a large free carrier density. It is generally accepted that these free carriers are generated by two mechanisms: (1) Sn atom substitution of indium atoms which supplies an extra electron, and two oxygen vacancies which act as two electron donors [31].

The Indium–Tin phase diagram shows one eutectic point at 117°C (46% Sn) very similar to on of InBi (110°C, 53% Bi) the eutectic near the InBi composition.

XRD analysis reveals that sputter-deposited at high substrate temperature at range of (300-500°C). $In_2O_3$:Sn films consist of various sizes of $In_2O_3$ crystalline grains (10-50 nm) [33] with different orientations. At lower temperature($< 150°C$) transmission electron microscopy shows a crystallite size $\geq$ 50 nm.

As determined by XRD, the as-deposited ITO films are amorphous. The crystallization process begins at 270°C. The films are fully crystallized by 300°C.

The substrate crystallinity significantly affect the electrical and optical properties of ITO films. The conductivity of ITO films grows as the substrate deposition temperature increases, as measured by hall measurements and four point probe. The grain size gets larger with increasing growth temperature. Optical transmittance also increases with increase in the grain size of the films. It is observed that the average optical transmittance ($T_a$) increases from 83% to 87% with increasing substrate temperature from 25°C to 300°C [33].

In most cases the substrate used for deposition of the film in different cases affects the texture of the films. Heat treatments in controlled atmosphere can improve the performance of $In_2O_3$:Sn.

To prepare ITO films, various deposition techniques have been used, but the most common is co-sputtering in oxygen. In order to obtain the highest quality ITO films, these techniques require either a high substrate temperature (300-500°C) during deposition or a post-deposition annealing treatment of the films at high temperature (400-700°C) [33]. ITO

thin films in commercial use are mostly amorphous, heated to lower temperatures (300°C) to preserve commonly used glass substrates. The electrical properties of the ITO films depends on the composition of $SnO_2$ [33]

The oxygen deposition pressure is one of the other important parameters affecting transparency and conductivity of the ITO films. Decreasing the oxygen pressure increases the number of oxygen vacancies in the lattice, which increases the carrier concentration and film conductivity. These observations showed that oxygen pressure can affect the transparency increasing the free carrier absorption. The surface roughness of the ITO is important to the performance of devices. Atomic Force Microscopy (AFM) measurement used to measure roughness of ITO films, finds a Root Mean Square (r.m.s.) surface roughness of $\sim$ 7 Å, for ITO films grown at room temperature [33] with a grain size of the ITO films observed to be 20 - 40 nm [33].

The direct band-gap ($E_g$) of ITO film is in the range of 3.89 eV to 4.21 eV depending on the substrate deposition temperature (25°C to 300°C) [33]. This shift of the band-gap referred to the absorption edge, shifts towards higher energy with an increase of carrier concentration [33]. The plasma wavelength (or cutoff wavelength) ($\lambda_P$), is defined as the $\lambda$ when Transmittance equals Reflectance, (where the dielectric-like transmission equals the metallic-like IR reflectance). It is observed to initially decrease with increasing substrate deposition temperature up to 100°C, and then slightly increase up to 300°C [33].

ITO as-deposited films, room-temperature co-sputtered with oxygen, have an amorphous structure and low temperature heat treatments gives partial crystallization. At higher temperatures ITO starts to fully crystallize. Too high deposition energy in the ITO case can destroy the crystalline phase and cause amorphization. Rapid heating and cooling for ITO does not maintain crystallize films [34].

Main purpose of these section is to compare our InBi oxide films hall measurement data with relative data for Indium Tin Oxide (ITO) films in the literature [31]. The Hall mobility and carrier concentration observed for IBO compare to those reported for ITO. For optimal conductivity, ITO films are 5-10 wt% $SnO_2$, typically 300 nm thick with a carrier concentration $\sim 10^{21}$ $cm^{-3}$ [33]. ITO on glass substrates has a surface sheet resistance $\sim$ 23.5 $V/cm^2$. The substrate temperature and oxygen pressure affect the conductivity of the ITO films. The Hall mobility was 8.25 $cm^2/Vs$ to 20.97 $cm^2/Vs$ for laser annealed BiIn film deposited on Si(001), $SiO_2$, or $Si_3N_4$, and 2.85 $cm^2/Vs$ for ITO deposited on Si(001). The

carrier concentration on the same samples showed a range of $2.17\times10^{20}$ - $3.87\times10^{20}cm^{-3}$. Further, the sheet resistance was 1.84 - 2.28 $cm^{-2}$.

Since a substitutional Bi or Sn ion in the $In_2O_3$ single phase would add electrons to the conduction band ITO and similarly IBO films are conductive.

ITO optical transmittance at 300 - 550 nm thick films is for $\lambda$=300 nm 85% [27]. The highest transmittance for laser annealed In/Bi films, is 78%.

## 4.3 Future Work

Furnace annealing at higher temperatures should be conducted in future, since the actual laser exposure temperature could have been much higher than 246°C. It is known at this moment that oxygen is a necessary part of the conversion of Bi/In to a transparent film. We suspect that water may have been a large contributor of the oxygen. Therefore, annealing in steam and water should be conducted in future. More Hall-effect measurements on patterned samples to study electrical properties in greater detail would be useful. Optical properties through band-gap energy measurements should be carried out and compared with ITO. Study what furnace temperature needed to approach transparency. More TEM measurements on laser-annealed samples deposited directly on grid.

# Bibliography

[1] Glenn Chapman, Yuqiang Tu, Marinko V. Sarunic, "Bi/In Bimetallic Thermal Resists for Microfabrication, Photomasks and Micromachining Applications", Proceedings SPIE Advances in Resist Technology and Processing XIX, 4690, 465-476 (2002).

[2] Glenn H. Chapman, Yuqiang Tu, Marinko V. Sarunic, "A Prototype Laser Activated Bimetallic Thermal Resist for Microfabrication", SPIE Proceedings Laser Applications in Microelectronics and Optoelectronics Applications, v 4274, pg 183-193, San Jose, CA 2001.

[3] J. S. Johnson, G.H. Chapman, N. Pfeiffer, "Economic Analysis of a Semiconductor Factory Satellite", submitted to AIAA Space 2000, Albuquerque, NM, March 2000.

[4] Marinko V. Sarunic, Glenn H. Chapman, Yuqiang Tu, "BiIn: a Sensitive Bimetallic Thermal Resist", Proceeding SPIE Advances in Resist Technology and Processing XVIII, Vol. 4345, 557-568, Santa Clara, CA Mar 2001.

[5] Y. Tu, G.H. Chapman, "Bi/In: A Novel Bimetallic Thermal Resists for Optical and Micromachining Applications", SPIE OptoCanada 2002, Abstract only published, Ottawa May 2002

[6] M.V. Sarunic, Master's Thesis "Bi/In: A prototype Bimetallic Laser Activated Thermal Inorganic Resist for Microlithography", School of Engineering Science, Simon Fraser University, (2001).

[7] BiIn-88 Che P Y Chevalier, Calphad 12 (1988) 4 p 383-392 (rev.1990).

[8] Y. Tu and G. Chapman, "Bi/In as Patterning and Masking Layers for Alkaline-Based Si Anisotropic Etching", presented at SPIE Photonics West-Micromachining and Microfabrication Session, San Jose, CA, 25 - 31 Jan, 2003.

[9] Y. Tu, G.H. Chapman, and M.V. Sarunic "Bimetalltic Thermall Activated films for Microfabrication, Photomasks and Data Storage", Proceedings SPIE Photonics West, Laser Applications in Microelectronics and Optoelectronics Applications, v4637, pg 330-340, San Josa, CA 2002.

[10] `http://www.espi-metals.com/msds's/bismuth.pdf.`
Bismuth MSDS, April 2003.

[11] `http://www.espi-metals.com/msds's/indium.pdf.` Indium MSDS: April 2003,

[12] BiIn-88 Che P Y Chevalier, Calphad 12(1988)4 p 383-392 (rev.1990).

[13] Carbon Doping of GaSb by Rodney David Wiersma M.Sc., Simon Fraser University, (2001).

[14] Torben M. Hansen,a) Kurt Stokbro, and Ole Hansen, Tue Hassenkam, Ichiro Shiraki, Shuji Hasegawa. "Resolution enhancement of scanning four-point-probe measurements on two-dimensional systems". Review of scientific instruments Volume 74, Number 8 August 2003

[15] David B. Williams, "Transmission Electron Microscope", Plenum Pr; 1996, pg 74.

[16] http://www.mastest.com/xrdxrr.htm

[17] http://materials.binghamton.edu/labs/xray/xray.html.

[18] David B.Williams and C. Barry Carter, Transmission Electron Microscopy and Diffractometry of Materials,1996 Plenum Press, New York page 356.

[19] P.J. Goodhew, J. Humphrey, R. Beanland, "Electron Microscopy and Analysis", New York, London, Taylor and Francis, Third Edition, 2001.

[20] William D. Callister, "Materials Science and Engineering, An Introduction", New York, Wiley, Fifth Edition, 2000.

[21] C. Jeynes, Z. H. Jafri, R. P. Webb, A. C. Kimber, and M. J. Ashwin, Surf. Interface Anal. 25, 254 1997.

[22] J. F. Ziegler and J. E. E. Baglin, J. Appl. Phys. 42, 2031, 1971.

[23] L. R. Doolittle, Nucl. Instrum. Methods Phys. Res. B 9, 291, 1985.

[24] L. J. van der Pauw. Philips Res. Repts, 13:1, 1958.

[25] Y. Tu, M. Karimi, N. Morawej, W. Lennard, J. Peng, K. L. Kavanagh, and G. H. Chapman, "Wavelength Invariant Resist Composed of Bimetallic Layers", Proc. Novel Materials and Processes for Advanced CMOS Symposium , Materials Research Soc. Conf., v745, pg 73-78, Boston, Dec. 2002

[26] G. Kiriakidis, H. Ouacha and N. Katsarakis, Rev. Adv. Mater. Sci. 4(2004) 32-40.

[27] Daeil Kim, Steven Kim, "Effect of ion beam energy on the electrical, optical, and structural properties of indium tin oxide thin films prepared by direct metal ion beam deposition technique", Thin Solid Films 408 (2002) 218-222.

[28] Chemical and Thin-Film Straetegies for New Transparent Conducting Oxides, 45 A. J. Freeman, K. R. Peoppelmeier, MRS Bulletin, Aug (2000).

[29] M.V. Sarunic, Master's Thesis "Bi/In: A prototype Bimetallic Laser Activated Thermal Inorganic Resist for Microlithography", School of Engineering Science, Simon Fraser University, (2001).

[30] Mat-wiss u. Werkstofftech. 34, 662-665(2003).

[31] X. W. Sun, D. H. Kim, LG Electronics, Seoul, Korea.

[32] Hansen, Constitution of Binary Alloys, 1958.

[33] H. Kim, J. S. Horwitz. Appl. Phys. A, **69** (1999), 4342.

[34] K. Zhang, F. Zhu, C. Huan, A. Wee, J. Appl. Phys. 86 (1999) 974.

[35] D. Vaufrey, M. Ben Khalifa, J. Tardy, C. Ghica, M. G. Blanchin, C. Sandu and J. A. Roger. "ITO-on-top organic light emitting devices: a correlated study of opto-electronic and structural characteristics" Semicond. Sci. Technol. 18(2003) 253-260.

# Appendix A

Details of X-ray and electron diffraction analysis are shown in the tables to fallow. Each table is associated with a particular XRD spectrum or selected area diffraction pattern in the Results chapter.

Table A.1: Summary and analysis of X-ray data from Fig. 3.1 0.9W laser-annealed BiIn thin films (12/12 nm) on Si (001). The database numbers are from JCPDS-ICDD (1993).

| $2\theta$ | Int. | d spacing | Phase | | | | |
|---|---|---|---|---|---|---|---|
| (Degree) | Norm. | | $Bi_2O_3$ | $Bi_2O_{2.33}$ | $In_2O_3$ | $In_2O_3$ | $\beta$-$Bi_2O_3$ |
| | | | 41-1449 | 27-51 | 22-336 | 6-416 | 27-50 |
| 15.61 | 1.69 | 5.67 | | 0 0 6 | | | |
| 20.22 | 2.05 | 4.39 | | 0 0 8 | | | |
| 21.93 | 3.14 | 4.05 | 0 2 0 | | | | |
| 28.21 | 100.00 | 3.16 | | | | | 2 0 1 |
| 31.10 | 14.23 | 2.87 | | | 1 0 4 | | |
| 33.03 | 2.17 | 2.71 | | | | 3 2 1 | |
| 35.96 | 4.70 | 2.49 | | 1 1 6 | | | |
| 37.43 | 0.36 | 2.40 | | | 0 0 6 | | |
| 38.14 | 1.33 | 2.36 | | | 1 1 3 | | |
| 39.61 | 0.48 | 2.27 | | | | 2 0 2 | |
| 42.23 | 1.33 | 2.14 | 3 3 2 | | | | |
| 46.13 | 1.33 | 1.97 | | | | 4 3 9 | |
| 51.71 | 2.41 | 1.77 | | | | 4 4 0 | |
| 57.99 | 4.70 | 1.59 | | | 2 1 4 | | |
| 61.38 | 2.90 | 1.51 | | | | 6 2 2 | |
| 64.27 | 1.57 | 1.45 | | | 2 0 8 | | |
| 69.13 | 4.37 | 1.36 | Si (0 0 4) | | | | |
| 76.36 | 0.60 | 1.25 | | | 1 2 8 | | |
| 78.77 | 1.45 | 1.21 | 1 1 2 | | | | |

Table A.2: Summary and analysis of the XRD data from Fig. 3.1 Bi/In films on Si(001), (a) as-deposited, (b) 2.5 W , and (c) 3.2W laser-annealed sample. Data calibration based on the Si(004) peak. The database are from JCPDS-ICDD (1993).

| $2\theta$ | | | Int. | d | phase | | | |
|---|---|---|---|---|---|---|---|---|
| (Degrees) | | | Norm. | | BiIn | $BiIn_2$ | $Bi_2O_3$ | $In_2O_3$ |
| As-dep. | 2.5W | 3.2W | | | 32-113 | 11-566 | 41-1449 | 6-416 |
| 18.64 | | | 25 | 4.72 | 0 0 1 | | | |
| 26.12 | | | 35 | 3.41 | 1 0 1 | | | |
| 27.24 | | | 12 | 3.27 | | 0 0 2 | | |
| | 27.74 | 27.74 | 38 | 3.21 | $\delta$-$Bi_2O_3$(1 1 1) | | | |
| 27.98 | | | 9 | 3.19 | $Bi_3In_5$(004) | | | |
| | 30.86 | 30.86 | | | | | 0 0 12 | 2 2 2 |
| 32.72 | | | 12 | 2.73 | | 1 1 0 | | |
| | 32.95 | 32.95 | 45 | 2.72 | $In_2O_3$(22-336)(1 1 0) | | | |
| 33.10 | | | 16 | 3 | 0 0 2 | | | |
| | 34.20 | 34.20 | 29 | 2.62 | $Bi_2O_{2.33}$(1 1 4) | | | |
| | | 35.57 | 20 | 2.70 | $\delta$-$Bi_2O_3$(0 0 14) | | | |
| 37.80 | | | 100 | 2.52. | | 0 0 2 | | |
| 42.00 | | | 13 | 2.15 | 1 0 2 | | | |
| 42.90 | | | 4 | 2.11 | | 112 | | |
| 47.20 | | | 5 | 1.92 | | 2 0 2 | | |
| | 51.27 | | 21 | 1.78 | $\beta$-$Bi_2O_3$(411) | | | |
| 58.10 | | | 33 | 1.59 | | 3 0 0 | | |
| 61.23 | | | 10 | 1.51 | 3 1 1 | | | |
| | 61.72 | | 17 | 1.50 | | | | 6 2 2 |

Table A.3: Summary of the data from Fig. 3.2 as-deposited BiIn thin film (45/45 nm) on (Si(001), Si(111), $SiO_2$/Si(001), and $Si_3N_4$/Si(001). The database numbers are from JCPDS-ICDD (1993).

| 2θ | Int. | d | Phase | | | |
|---|---|---|---|---|---|---|
| (Degree) | Norm. | | BiIn | $BiIn_2$ | $Bi_3In_5$ | Bi |
| | | | 32-113 | 11-566 | 23-850 | 5-519 |
| 18.9 | 11 | 4.69 | 0 0 1 | | | |
| 23.06 | 2 | 3.86 | | 101 | | |
| 25.32 | 10 | 3.51 | 1 0 1 | | | |
| 26.07 | 48 | 3.41 | | 0 0 2 | | |
| 27.28 | 17 | 3.27 | | | 0 0 4 | |
| 28.65 | 17 | 3.07 | | | 2 2 0 | |
| 31.45 | 111 | 2.82 | 1 1 1 | | | |
| 32.54 | 19 | 2.72 | | 1 1 0 | | |
| 33.4 | 52 | 2.68 | | 1 0 2 | | |
| 36.04 | 30 | 2.49 | $Bi_{0.06}In_{0.94}$(0 0 2) | | | |
| 37.65 | 6 | 2.37 | 0 0 2 | | | |
| 41.91 | 12 | 2.15 | 1 0 2 | | | |
| 44.64 | 6 | 2.09 | 2 1 1 | | | |
| 45.76 | 7 | 2.06 | | | | 1 1 3 |
| 51.61 | 7 | 1.76 | 2 2 0 | | | |
| 52.89 | 9 | 1.72 | 2 0 2 | | | |
| 56.25 | 10 | 1.63 | 2 1 2 | | | |
| 58.50 | 5 | 1.59 | 0 0 3 | | | |
| 60.83 | 5 | 1.55 | 1 0 3 | | | |
| 61.63 | 10 | 1.50 | | | 3 1 1 | |
| 69.13 | 59 | 1.36 | Si(0 0 4) | | | |
| 69.97 | 16 | 1.34 | | 4 0 0 | | |
| 72.85 | 32 | 1.30 | 2 1 3 | | | |

Table A.4: Summary and analysis of X-ray data from Fig. 3.3 laser-annealed, BiIn thin film (45/45 nm) on silicon substrates Si (001), Si(111), $SiO_2$/Si (001), $Si_3N_4$/Si (001) and glass. The database are from JCPDS-ICDD (1993).

| 2θ(Si) | 2θ | Int | d | Phase | | | | |
|---|---|---|---|---|---|---|---|---|
| (Deg.) | (Deg.) | Norm. | | BiO | $Bi_2O_3$ | δ-$Bi_2O_3$ | $In_2O_3$ | $In_2O_3$ |
| | | | | 27-54 | 41-1449 | 27-52 | 22-336 | 6-416 |
| 12.40 | | 82 | 7.1 | $Bi_2O_{2.33}$(0 0 14) | | | | |
| 23.10 | | 100 | 3.82 | | | 1 1 0 | | |
| 25.29 | | 54 | 3.48 | | 0 0 2 | | | |
| | 26.29 | 52 | 3.35 | | 1 0 3 | | | |
| 27.91 | | 100 | 3.16 | 1 0 1 | | | | |
| | 29.78 | 62 | 2.96 | | | | | 2 2 2 |
| | 34.72 | 34 | | | | | | 4 0 0 |
| 36.62 | | 47 | 2.41 | | 1 1 2 | | | |
| | 37.19 | 76 | 2.37 | | | | 1 1 3 | |
| | 38.83 | 100 | 2.27 | | | | 2 0 2 | |
| 39.78 | | 32 | 2.21 | | 1 3 1 | | | |
| 41.75 | | 25 | 2.11 | | 1 2 2 | | | |
| | 47.88 | 56 | 1.84 | $Bi_2O_{2.33}$ (1 1 14) | | | | |
| | 50.24 | 27 | 1.76 | | | | 1 2 2 | |
| 54.82 | | 78 | 1.61 | | | | 2 4 1 | |
| | 55.39 | 28 | 1.59 | | | | 3 0 0 | |
| 57.12 | | 21 | 1.54 | | | | | 6 2 2 |
| | 63.92 | 12 | 1.38 | | | | 2 2 0 | |
| 69.13 | | 437 | 1.36 | Si (0 0 4) | | | | |
| | 71.33 | 8 | 1.23 | 1 1 6 | | | | |

Table A.5: Summary and analysis of X-ray data from Fig. 3.4 as-deposited Bi/In on Si (001) (45/45 nm). The data calibration is based on Si (004) or Si (111) peak positions. The database numbers are from JCPDS-ICDD (1993).

| 2θ | Int. | d | phase | | | |
|---|---|---|---|---|---|---|
| (degrees) | Norm. | | BiIn | $BiIn_2$ | $Bi_3 In_5$ | $In_2O_3$ |
| | | | 32-113 | 11-566 | 23-850 | 22-336 |
| 22.40 | 33 | 3.96 | | | | 0 1 2 |
| 27.37 | 100 | 3.25 | | 0 0 2 | | |
| 28.65 | 47 | 3.11 | | | 0 0 4 | |
| 30.18 | 49 | 2.96 | | | 2 2 0 | |
| 31.43 | 63 | 2.84 | 1 1 1 | | | |
| 34.23 | 37 | 2.62 | | 1 0 2 | | |
| 35.98 | 27 | 2.49 | 2 0 0 | | | |
| 38.13 | 35 | 2.36 | 0 0 2 | | | |
| 41.98 | 27 | 2.15 | 1 0 2 | | | |
| 44.99 | 27 | 2.01 | 2 1 1 | | | |
| 45.63 | 25 | 1.99 | 1 1 2 | | | |
| 47.78 | 27 | 1.90 | | | 2 0 6 | |
| 48.46 | 16 | 1.88 | | | 4 1 3 | |
| 51.47 | 27 | 1.77 | 4 0 4 | | 2 2 0 | |
| 53.18 | 33 | 1.72 | 2 0 2 | 2 1 2 | | |
| 54.03 | 18 | 1.70 | | | 5 1 0 | |
| 56.44 | 24 | 1.63 | 2 1 2 | 0 0 4 | 2 1 7 | |
| 59.44 | 16 | 1.55 | 3 0 1 | 2 1 2 | 1 1 8 | |
| 61.78 | 55 | 1.50 | 4 0 6 | | 3 1 1 | |
| 63.33 | 27 | 1.47 | | | 3 3 6 | |
| 69.13 | 333 | 1.36 | 3 0 2 | 2 2 0 | 4 1 7 | |
| 74.48 | 55 | 1.27 | | 2 2 2 | 4 0 8 | |
| 77.08 | 24 | 1.24 | 4 0 0 | | 3 3 8 | |
| 77.49 | 37 | 1.23 | | 6 1 5 | 3 1 2 | |

Table A.6: Summary and analysis of XRD measurements of as-deposited (45/45 nm -90/90 nm) Bi/In for 3 substrates (glass, Si(001), Si(111) Fig. 3.4. Calibration based on the substrate Si(004). The database numbers are from JCPDS-ICDD (1993).

| 2θ | | | Phase | | | | |
|---|---|---|---|---|---|---|---|
| Degrees | | | BiIn | $BiIn_2$ | $Bi_3In_5$ | Bi | In |
| | | | 32-113 | 11-566 | 23-850 | 5-519 | 5-642 |
| Si(001) | glass | Si(111) | | | | | |
| 18.80 | | | 0 0 1 | | | | |
| | 22.47 | | | | | 0 0 3 | |
| | 23.23 | | | 1 0 1 | | | |
| | 24.86 | | | 1 1 0 | | | |
| | 24.95 | 24.95 | 1 0 1 | | | | |
| | 25.29 | 25.29 | 1 1 0 | | | | |
| | 25.52 | 25.52 | 1 0 1 | | | | |
| | 27.15 | | 0 1 2 | | | | |
| | | 27.37 | | 1 0 1 | | | |
| | | 28.15 | Silicon (1 1 1) | | | | |
| | 30.63 | | 1 1 1 | | | | |
| | | 31.62 | | | 2 1 3 | | |
| 32.89 | | 32.82 | | 1 0 2 | | | |
| | | 33.36 | | | 3 1 0 | | |
| | | 36.06 | | | | | 0 0 2 |
| 37.93 | 37.93 | 37.93 | | | | 0 0 2 | |
| | 39.57 | | 2 0 1 | | | | |
| | | 43.06 | | 1 1 2 | | | |
| | 44.48 | | | | | 2 0 3 | |
| | | 44.91 | | | 3 3 0 | | |
| | | 45.79 | | 1 0 3 | | | |
| | | 47.30 | | | 3 3 2 | | |
| | 47.82 | | | | | 2 0 2 | |
| | 51.01 | | 2 2 0 | | | | |
| | | 51.77 | | | 4 0 4 | | |

| 2θ | | | Phase | | | | |
|---|---|---|---|---|---|---|---|
| Degree | | | BiIn | $BiIn_2$ | $Bi_3In_5$ | Bi | In |
| | | | 32-113 | 11-566 | 23-850 | 5-519 | 5-642 |
| Si(001) | glass | Si(111) | | | | | |
| | | 53.19 | | 2 1 2 | | | |
| | 56.02 | | | | | 0 2 4 | |
| | | 56.13 | 3 1 0 | | | | |
| 58.09 | | | 0 0 3 | | | | |
| 59.07 | | 59.07 | 3 1 3 | | | | |
| | 59.18 | | | 1 0 3 | | | |
| | 60.49 | | | | 1 1 8 | | |
| 61.58 | | | 3 1 1 | | | | |
| 61.65 | | | 2 0 5 | | | | |
| | | 61.79 | | | 4 0 6 | | |
| | 62.12 | | 2 2 2 | | | | |
| | 64.52 | | 3 0 2 | | | | |
| | | 66.47 | 3 2 1 | | | | |
| | | 68.44 | | 2 2 0 | | | |
| 69.35 | | | Silicon (0 0 4) | | | | |

Table A.7: Summary and analysis of XRD measurements from laser-annealed Bi/In of Fig. 3.5 for 3 substrates (glass, Si(001), Si(111)) in different fabrication time. Data calibration based on Si peak. The database numbers are from JCPDS-ICDD (1993).

| 2θ | | | Phase | | | | | |
|---|---|---|---|---|---|---|---|---|
| (Degrees) | | | $Bi_2O_3$ | $Bi_2O_{2.33}$ | δ-$Bi_2O_3$ | β-$Bi_2O_3$ | $In_2O_3$ | $In_2O_3$ |
| Si(001) | glass | Si(111) | 41-1449 | 27-51 | 27-52 | 27-50 | 6-416 | 22-336 |
| | | 16.76 | 0 1 1 | | | | | |
| | | 17.51 | | | | | 2 0 6 | |
| 18.80 | | | BiIn (0 0 1) | | | | | |
| | | 19.75 | -1 1 1 | | | | | |
| 21.60 | 21.50 | | | | | | 2 1 1 | |
| | | 22.45 | | | 1 1 0 | | | |
| | | 23.80 | | 1 0 1 | | | | |
| | | 24.95 | | 1 0 3 | | | | |
| | | 25.70 | -1 0 2 | | | | | |
| | | 27.00 | 1 2 0 | | | | | |
| 27.15 | 27.21 | | | | 1 1 1 | | | |
| 31.30 | 31.28 | | | 0 0 12 | | | | |
| 34.50 | | | | | | | | 1 1 0 |
| 35.70 | 35.74 | | | 0 0 14 | | | | |
| 37.70 | 37.95 | | Bi(1 0 4) | | | | | |
| | 39.95 | | | | | | | 2 0 2 |
| | | 43.74 | | | | | 4 2 2 | |
| | | 44.55 | | | | | | 1 1 6 |
| | 45.3 | | | | 2 2 0 | | | |
| | 45.85 | | | | | | | 0 2 4 |
| 45.89 | | | Bi(0 0 6) | | | | | |
| | 48.20 | | | 1 1 2 | | | | |
| 51.30 | 51.40 | | | | | | | 2 1 1 |
| | | 55.75 | Bi(0 2 4) | | | | | |
| 57.15 | | | | | | | | 1 2 2 |
| | 58.20 | | | | | | | 1 0 7 |
| | 62.12 | | | | | 4 3 1 | | |
| | 64.50 | | | | | | | 0 2 4 |
| | 64.70 | | | | | | | 2 0 8 |
| 69.35 | | | Silicon (0 0 4) | | | | | |

Table A.8: X - ray summary and analysis of low temperature bulk melt of Bi and In in $N_2$, Bi and In pieces melted at 270°C . The database numbers are from JCPDS-ICDD (1993).

| 2θ | Int. | d | Phase | | | |
|---|---|---|---|---|---|---|
| (Degree) | Norm. | Å | BiIn | $BiIn_2$ | $Bi_3In_5$ | Bi |
| 23.31 | 553 | 3.81 | | 1 0 1 | | |
| 23.77 | 656 | 3.74 | | | | 1 0 1 |
| 25.54 | 2202 | 3.48 | 1 1 0 | | | |
| 26.13 | 1743 | 3.41 | 1 0 1 | | | |
| 28.83 | 690 | 3.09 | | 2 2 0 | | |
| 31.88 | 2531 | 2.80 | 1 1 1 | | 2 1 3 | |
| 33.53 | 739 | 2.67 | | 1 0 2 | | |
| 36.23 | 720 | 2.48 | 2 0 0 | | | |
| 38.23 | 378 | 2.35 | 0 0 2 | | | |
| 40.79 | | 2.21 | 2 0 1 | | | |
| 42.23 | 464 | 2.14 | 1 0 2 | | | |
| 45.05 | 460 | 2.01 | 2 1 1 | | | |
| 46.93 | 336 | 1.93 | | 2 0 2 | | |
| 51.99 | 1239 | 1.76 | 2 2 0 | | | |
| 53.43 | 301 | 1.71 | 2 0 2 | | | |
| 56.69 | 412 | 1.62 | 2 1 2 | | | |
| 61.96 | 383 | 1.50 | 3 1 1 | | | |
| 71.09 | 1.32 | 3 1 2 | | | | |
| 84.77 | 212 | 1.14 | 3 0 3 | | | |
| 87.23 | 192 | 1.12 | 3 3 1 | | | |
| 32.29 | | 2.77 | | 1 1 0 | | |
| 51.43 | | 1.77 | 2 2 0 | | | |
| 57.2 | | 1.61 | 2 1 2 | | | |
| 62.18 | | 1.49 | 3 1 1 | | | |
| 71.43 | | 1.32 | 3 1 2 | | | |
| 73.63 | | 1.29 | 2 1 3 | | | |

Table A.9: XRD summary and analysis of heated BiIn (50 %) solid metals in air, at 270°C. The database numbers are from JCPDS-ICDD (1993).

| 2θ | d | Phase | | | | | | |
|---|---|---|---|---|---|---|---|---|
| (Deg.) | Å | BiO | $Bi_2O_3$ | $Bi_2O_{2.33}$ | δ-$Bi_2O_3$ | β-$Bi_2O_3$ | $In_2O_3$ | $In_2O_3$ |
| | | 27-54 | 41-1449 | 27-51 | 27-52 | 27-50 | 22-336 | 6-416 |
| 22.17 | 4.01 | | 0 2 0 | | | | | |
| 28.43 | 3.14 | 1 0 1 | | | | | | |
| 28.77 | 3.10 | | | 1 0 7 | | | | |
| 30.63 | 2.92 | | | | | | | 2 2 2 |
| 31.15 | 2.87 | | | | | | 1 0 4 | |
| 32.84 | 2.72 | | | | | | 1 1 0 | |
| 33.69 | 2.66 | | 2 0 0 | | | | | |
| 35.85 | 2.50 | | | | | | | 4 0 0 |
| 36.9 | 2.43 | | | | | | 0 0 6 | |
| 37.43 | 2.40 | | | | | | | 4 1 1 |
| 38.43 | 2.34 | | | | | 3 0 1 | | |
| 0.03 | 2.25 | 0 1 2 | | | | | | |
| 41.98 | 2.15 | | | | | | | 3 3 2 |
| 46.22 | 1.96 | | | | | | 0 2 4 | |
| 46.54 | 1.95 | | | | 2 2 0 | | | |
| 49.43 | 1.84 | | 3 1 2 | | | | | |
| 49.94 | 1.82 | | | | | | 1 1 6 | |
| 51.63 | 1.77 | | | | | | | 4 4 0 |
| 55.01 | 1.67 | 1 1 3 | | | | | | |
| 56.53 | 1.63 | | | | | 4 2 1 | | |
| 57.33 | 1.61 | | | | | | 2 1 4 | |
| 61.26 | 1.51 | | | | | | | 6 2 2 |
| 62.68 | 1.48 | | 1 5 1 | | | | | |
| 63.63 | 1.46 | | | | | | 2 0 8 | |
| 65.83 | 1.42 | | 0 0 4 | | | | | |
| 67.7 | 1.38 | 0 2 4 | | | | | | |
| 68.71 | 1.36 | | | | | | 2 2 0 | |
| 69.53 | 1.35 | | | | | | 3 0 6 | |

| 2θ | d | Phase | | | | | | |
|---|---|---|---|---|---|---|---|---|
| (Deg.) | Å | BiO | $Bi_2O_3$ | $Bi_2O_{2.33}$ | δ-$Bi_2O_3$ | β-$Bi_2O_3$ | $In_2O_3$ | $In_2O_3$ |
| | | 27-54 | 41-1449 | 27-51 | 27-52 | 27-50 | 22-336 | 6-416 |
| 74.43 | 1.27 | | | | | | 1 2 8 | |
| 75.63 | 1.26 | 2 1 1 | | | | | | |
| 77.01 | 1.24 | 1 1 6 | | | | | | |
| 80.43 | 1.19 | 1 1 2 | | | | | | |
| 82.43 | 1.17 | 0 1 8 | | | | | | |
| 83.78 | 1.15 | 0 1 8 | | | | | | |
| 86.49 | 1.12 | 3 0 0 | | | | | | |

Table A.10: Electron diffraction pattern analysis of the SAD data in Fig. 3.8. Data calibration was based on a GaAs sample. The phase database numbers are from JCPDS-ICDD (1993).

| Radius | Int. | d | BiIn | $BiIn_2$ | $Bi_3In_5$ |
|---|---|---|---|---|---|
| mm | | Å | 32-113 | 11-566 | 23-850 |
| 3.30 | Dark | 5.93 | | | |
| 7.20 | 10.00 | 2.72 | | 1 1 0 | |
| 8.10 | 0.5 | 2.41 | 0 0 2 | | |
| 9.2 | 5.00 | 2.13 | | | 0 0 6 |
| 10.00 | 5.00 | 1.96 | | 2 0 2 | |
| 11.40 | 2.00 | 1.72 | 2 2 0 | | |
| 12.20 | 1.00 | 1.60 | 0 0 3 | 0 0 4 | |
| 13.1 | 7.00 | 1.49 | 3 1 1 | | |
| 14.00 | 1.00 | 1.40 | 2 2 2 | | |
| 15.60 | 1.00 | 1.25 | 4 0 0 | | |
| 17.00 | 1.00 | 1.15 | 3 0 3 | | |
| 18.40 | 1.00 | 1.06 | | 2 2 4 | |
| 19.50 | 0.5 | 1.00 | | | 8 0 2 |

Table A.11: (b) Analysis of the SAD shown in Fig. 3.9. Furnace-annealed 150°C on SiO grid. The database numbers are from JCPDS-ICDD (1993).

| Radius | Intensity | d-spacing | BiO | $Bi_2O_3$ | $\delta$-$Bi_2O_3$ | $In_2O_3$ | $In_2O_3$ |
|---|---|---|---|---|---|---|---|
| mm | | Å | 27-54 | 41-1449 | 27-51 | 6-416 | 22-336 |
| 3.50 | Dark | 5.13 | | | | 2 0 0 | |
| 5.00 | 8.00 | 3.59 | $Bi_2O_{2.33}$ 1 0 3 | | | | |
| 6.20 | 050 | 2.90 | | | | | 1 0 1 |
| 7.00 | 10.00 | 2.57 | | | | 4 0 0 | |
| 8.10 | 3.00 | 2.22 | | | | | 2 0 2 |
| 9.40 | 3.00 | 1.91 | | 2 0 0 | | | |
| 10.30 | 2.00 | 1.74 | | | | 4 4 0 | |
| 11.40 | 8.00 | 1.58 | | | | | 2 1 4 |
| 12.50 | 1.00 | 1.44 | | | | | 2 0 8 |
| 13.30 | 9.00 | 1.35 | | | | | 2 2 0 |
| 14.70 | 1.00 | 1.22 | 2 1 1 | | | | |
| 16.10 | 1.00 | 1.05 | 4 2 2 | | | | |
| 17.10 | 1.00 | 1.05 | 3 0 3 | | | | |
| 17.50 | 1.00 | 1.03 | | | 4 4 0 | | |
| 18.00 | 1.00 | 1.00 | | | 5 3 1 | | |
| 18.90 | 1.00 | 0.95 | | | 6 2 0 | | |

Table A.12: (c)Analysis of the SAD shown in Fig. 3.10. Furnace-annealed sample at 200 °C on SiO grid. The database numbers are from JCPDS-ICDD (1993).

| Radius | Int. | d | BiO | $Bi_2O_3$ | δ-$Bi_2O_3$ | β-$Bi_2O_3$ | $In_2O_3$ | $In_2O_3$ |
|---|---|---|---|---|---|---|---|---|
| mm | Count | Å | 27-54 | 41-1449 | 27-51 | 27-52 | 6-416 | 22-336 |
| 3.50 | Dark | 5.73 | | | | | | |
| 4.4 | 0.5 | 4.08 | | | | | 2 1 1 | |
| 5.00 | 7 | 3.59 | $Bi_2O_{2.33}$ (1 0 3) | | | | | |
| 6.30 | 2.00 | 2.85 | | | | | 2 2 2 | |
| 7.00 | 10.00 | 2.57 | | | | | 4 0 0 | |
| 8.10 | 3.00 | 2.22 | | | | | | 2 0 2 |
| 8.50 | 3.00 | 2.11 | | | | | | 0 2 4 |
| 9.00 | 2.00 | 2.00 | | | | 2 2 2 | | |
| 9.60 | 3.00 | 1.87 | | | | | | 1 1 6 |
| 10.30 | 2.00 | 1.74 | | | | | 4 4 0 | |
| 11.40 | 8.00 | 1.58 | | | | | | 2 1 4 |
| 12.40 | 2.00 | 1.45 | | | | | | 2 0 8 |
| 13.50 | 8.50 | 1.33 | | | | | | 2 2 0 |
| 14.80 | 1.00 | 1.21 | 2 1 1 | | | | | |
| 15.5 | 0.3 | 1.16 | Bi (1 1 9) | | | | | |
| 16.20 | 1.00 | 1.11 | 4 2 2 | | | | | |
| 17.40 | 1.00 | 1.03 | | | 3 0 3 | | | |
| 18.00 | 1.00 | 1.00 | | | 4 4 0 | | | |
| 18.90 | 1.00 | 0.95 | | | 6 2 0 | | | |
| 19.80 | 1.5 | 0.91 | | | 6 0 0 | | | |

Table A.13: (d) Analysis of the SAD shown in Fig. 3.11. Furnace-annealed sample at 246 °C on SiO grid. The database numbers are from JCPDS-ICDD (1993).

| Radius | Int. | d | BiO | $Bi_2O_{2.33}$ | δ-$Bi_2O_3$ | β-$Bi_2O_3$ | $In_2O_3$ | $In_2O_3$ |
|---|---|---|---|---|---|---|---|---|
| mm | Count | Å | 27-54 | 27-51 | 27-52 | 27-50 | 6-416 | 22-336 |
| 3.20 | Dark | 6.27 | | | | | | |
| 4.00 | 1.00 | 4.49 | $Bi_2O_3$(1 1 1) | | | | | |
| 4.90 | 8.00 | 3.67 | | 1 0 3 | | | | |
| 5.60 | 1.00 | 3.21 | | | | 2 0 1 | | |
| 6.90 | 10.00 | 2.60 | | 1 1 4 | | | | |
| 7.70 | 2.00 | 2.33 | | | | | | 1 1 3 |
| 8.30 | 3.00 | 2.16 | | | | | 3 3 2 | |
| 9.10 | 3.00 | 1.97 | | | | | | 0 2 4 |
| 10.00 | 4.00 | 1.80 | | | | | | 1 1 6 |
| 11.20 | 5.00 | 1.60 | | | | | | 2 1 4 |
| 12.20 | 2.00 | 1.47 | | | | | 6 2 2 | |
| 13.00 | 6.00 | 1.38 | | | | | | 2 2 0 |
| 14.40 | 2.00 | 1.25 | | | | | | 1 2 8 |
| 15.5 | 3.00 | 1.16 | 0 1 8 | | | | | |
| 16.80 | 3.00 | 1.07 | 0 2 7 | | | | | |
| 18.10 | 3.00 | 0.99 | | | 4 4 0 | | | |
| 19.20 | 1.50 | 0.94 | | | 5 3 1 | | | |
| 20.40 | 1.5 | 0.88 | | | 6 2 0 | | | |
| 21.30 | 1.00 | 0.84 | | | 5 3 3 | | | |

Table A.14: (e) Analysis of the SAD shown in Fig. 3.12. Laser-annealed Bi/In on Si Ion milled.

| Radius | Intensity | d-spacing | $Bi_2O_3$ | δ-$Bi_2O_3$ | BiO | $In_2O_3$ |
|---|---|---|---|---|---|---|
| mm | Count | Å | 41-1449 | 27-51 | 27-54 | 22-336 |
| 3.50 | Dark | | | | | |
| 6.18 | 8.00 | 3.53 | 0 2 1 | | | |
| 6.34 | 6.00 | 3.44 | 0 0 2 | | | |
| 7.83 | 10.00 | 2.79 | | 2 0 0 | | 1 1 0 |
| 9.46 | 6.00 | 2.31 | $Bi_2O_{2.33}$(1 1 8) | | | 1 1 3 |
| 12.10 | 8.00 | 1.80 | | | | 1 1 6 |
| 14.05 | 10.00 | 1.55 | | | | 3 0 0 |
| 14.46 | 8.00 | 1.51 | $In_2O_3$(6-416) 6 2 2 | | | |
| 16.78 | 10.00 | 1.30 | | | | 3 1 2 |
| 17.27 | 4.00 | 1.26 | | | 2 1 1 | |
| 18.54 | 2.00 | 1.18 | | | 1 1 2 | |
| 20.01 | 1.00 | 1.09 | | | 0 0 9 | |
| 20.42 | 1.00 | 1.07 | | 5 1 1 | | |
| 22.32 | 1.00 | 0.88 | | 6 2 0 | | |